FIGURES

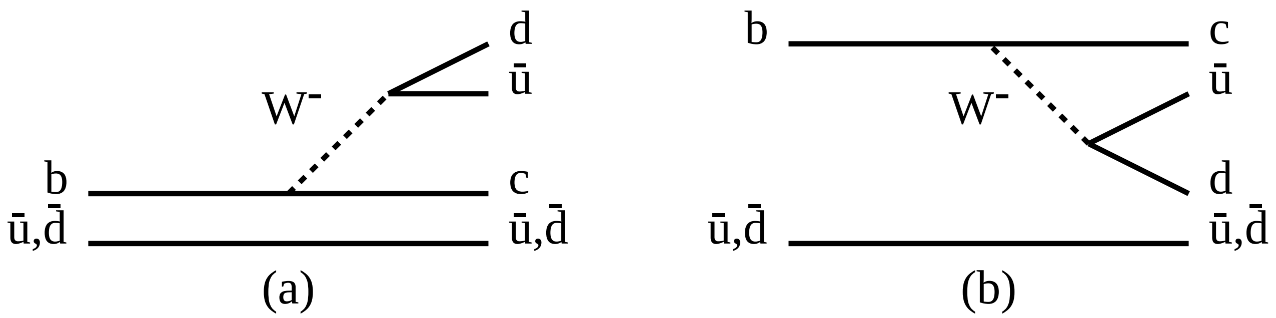

FIG. 1. B meson decay diagrams: (a) external spectator and (b) color suppressed.

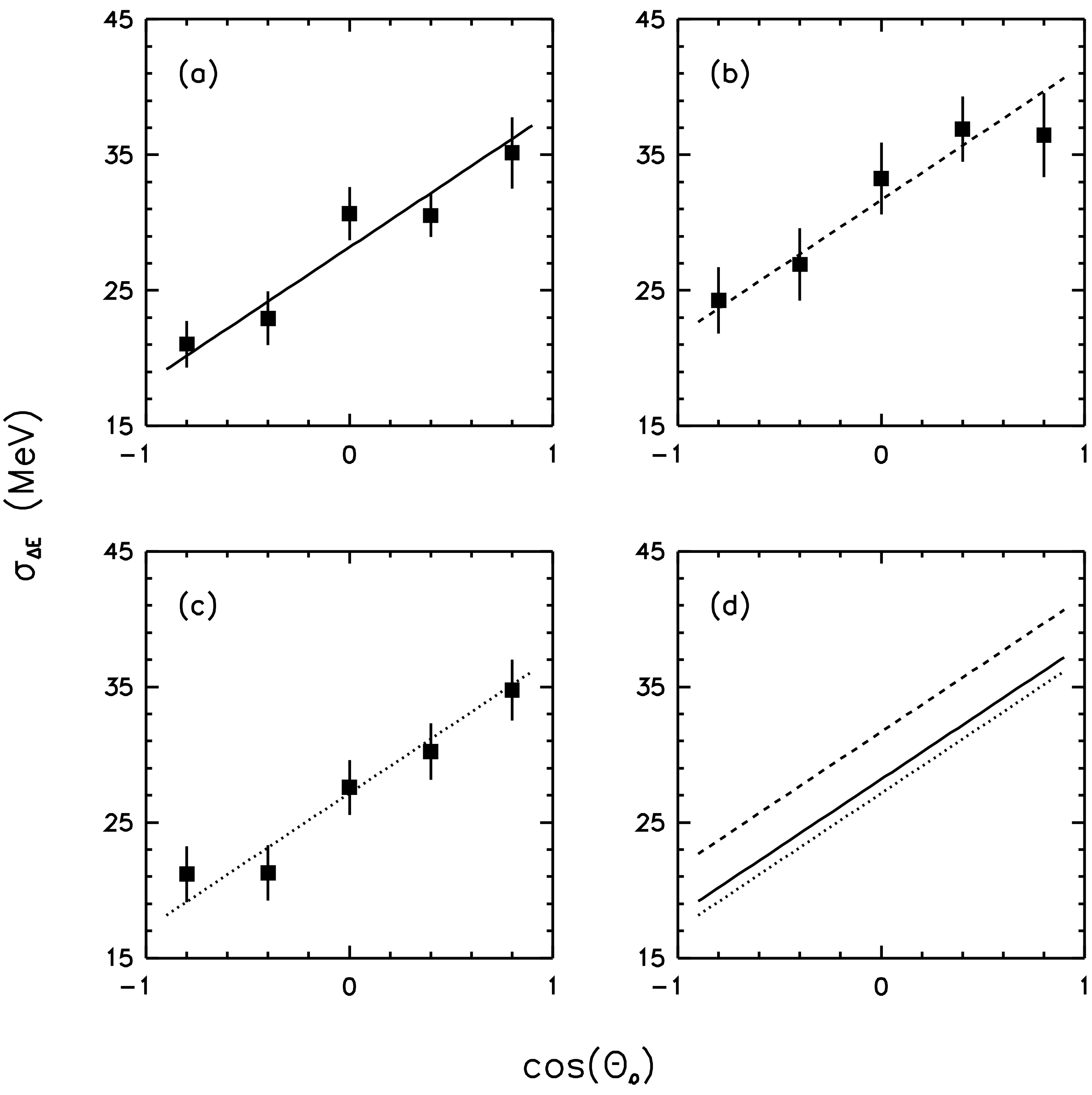

FIG. 2. Energy resolution as a function of the ρ^- helicity angle for the decay chains $B^- \to D^0\rho^-$, followed by (a) $D^0 \to K^-\pi^+$, (b) $D^0 \to K^-\pi^+\pi^0$ or (c) $D^0 \to K^-\pi^+\pi^-\pi^+$. The fits for all three modes are shown in (d).

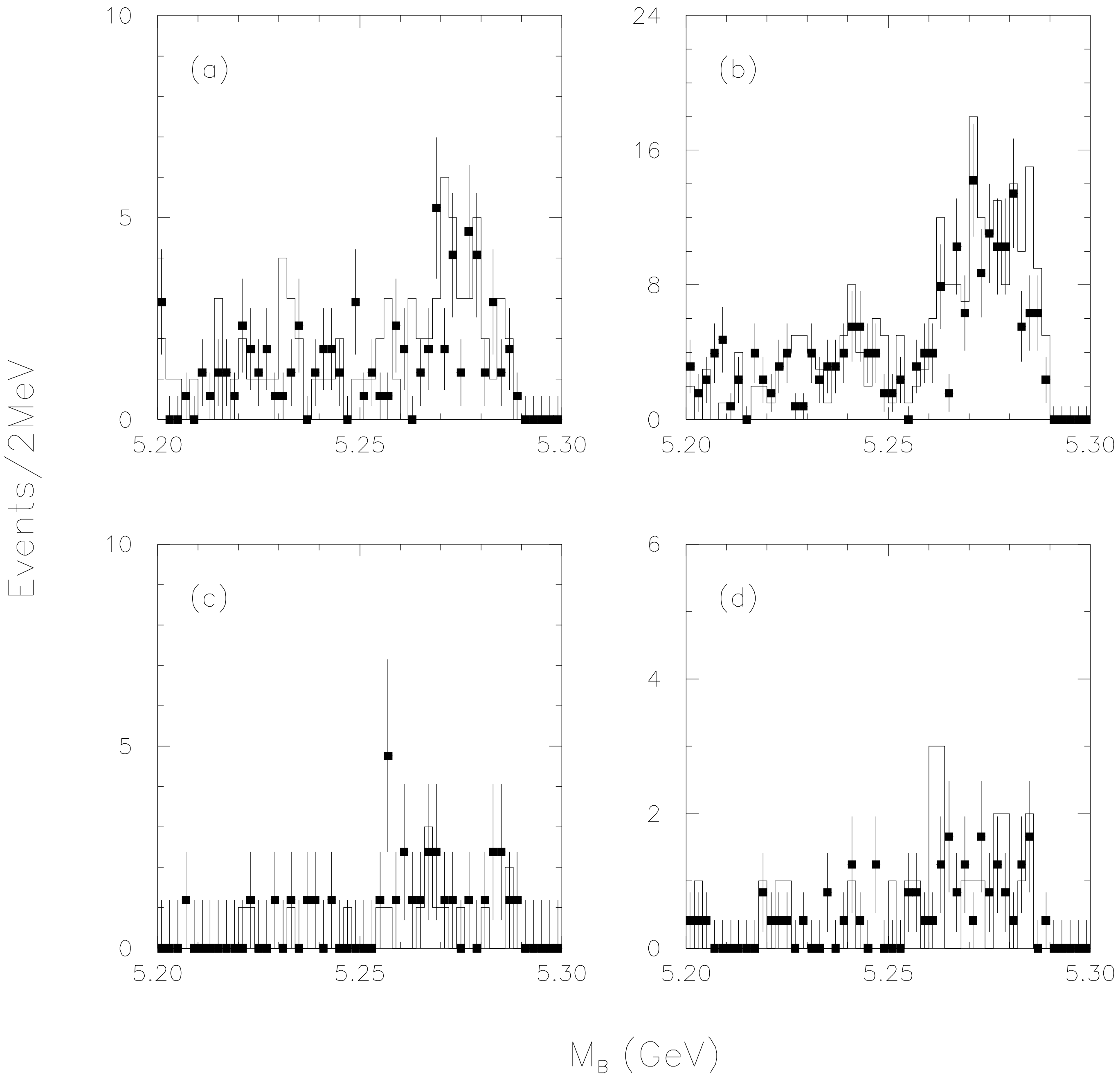

FIG. 3. A Monte Carlo simulation of the M_B distributions of $B\bar{B}$ background (solid histogram), compared with the ΔE sidebands from the same Monte Carlo (points). All events in the signal modes have been removed from the $B\bar{B}$ Monte Carlo simulation. (a) $B^- \to D^0\pi^-$, (b) $B^- \to D^0\rho^-$, (c) $B^- \to D^{*0}\pi^-$, and (d) $B^- \to D^{*0}\rho^-$.

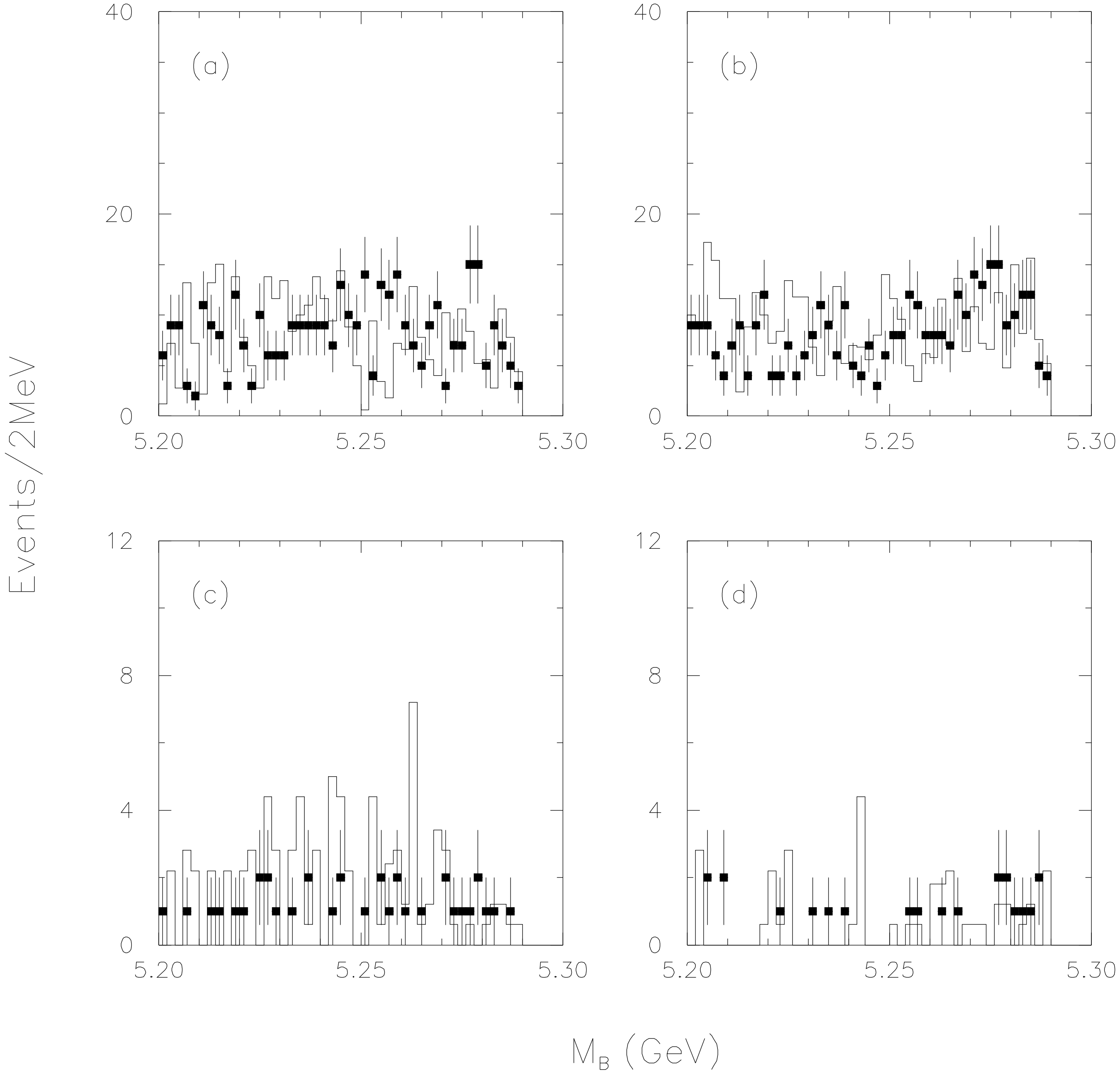

FIG. 4. M_B distributions for ΔE sidebands in on-resonance data (solid histogram) compared to the sum of continuum data and a Monte Carlo simulation of $B\bar{B}$ background (points) (a) $B^- \to D^0\pi^-$, (b) $B^- \to D^0\rho^-$, (c) $B^- \to D^{*0}\pi^-$, and (d) $B^- \to D^{*0}\rho^-$.

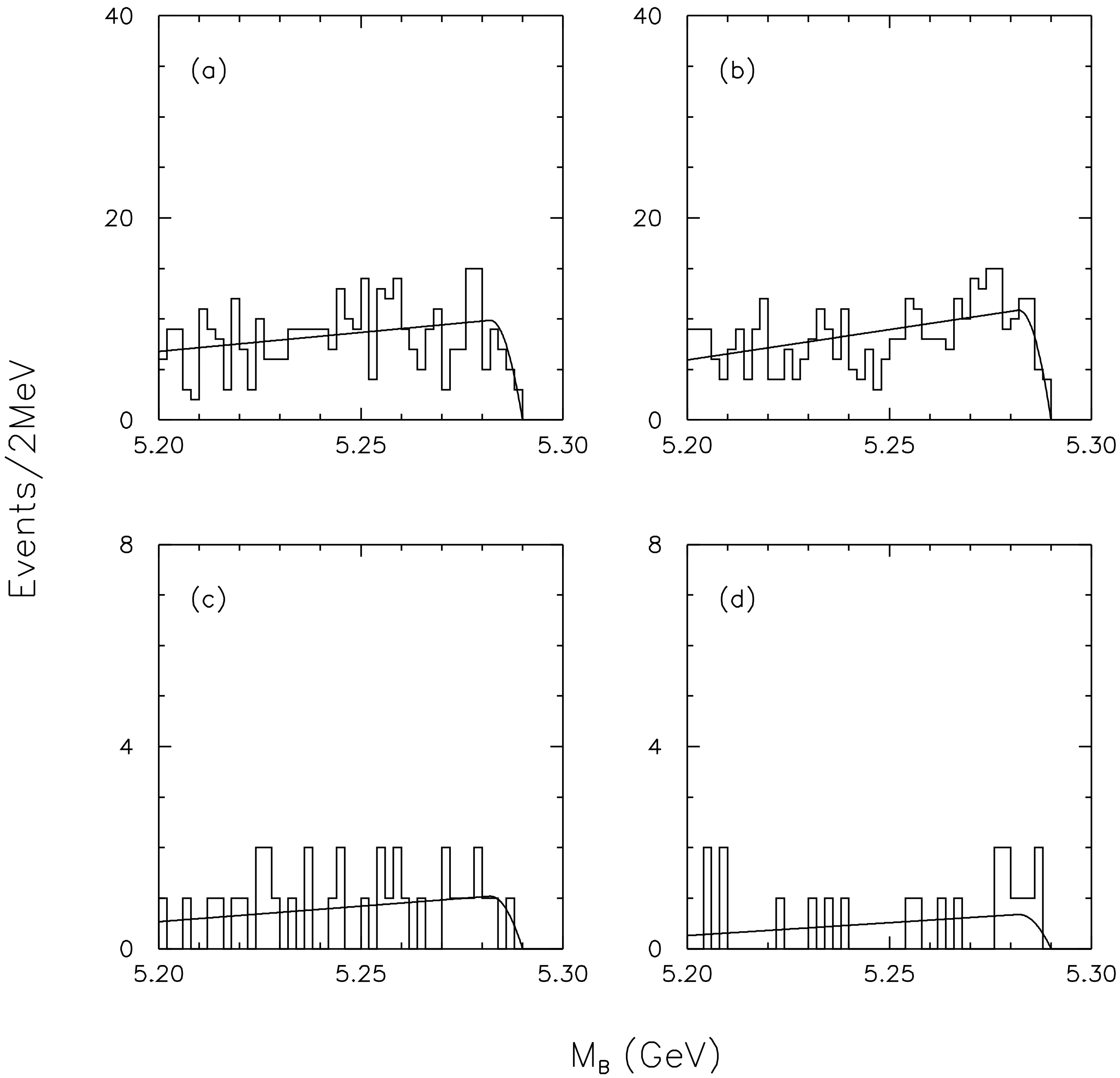

FIG. 5. M_B distributions for ΔE sidebands in data with a fit to the CLEO background shape superimposed: (a) $B^- \to D^0\pi^-$, (b) $B^- \to D^0\rho^-$, (c) $B^- \to D^{*0}\pi^-$ and (d) $B^- \to D^{*0}\rho^-$.

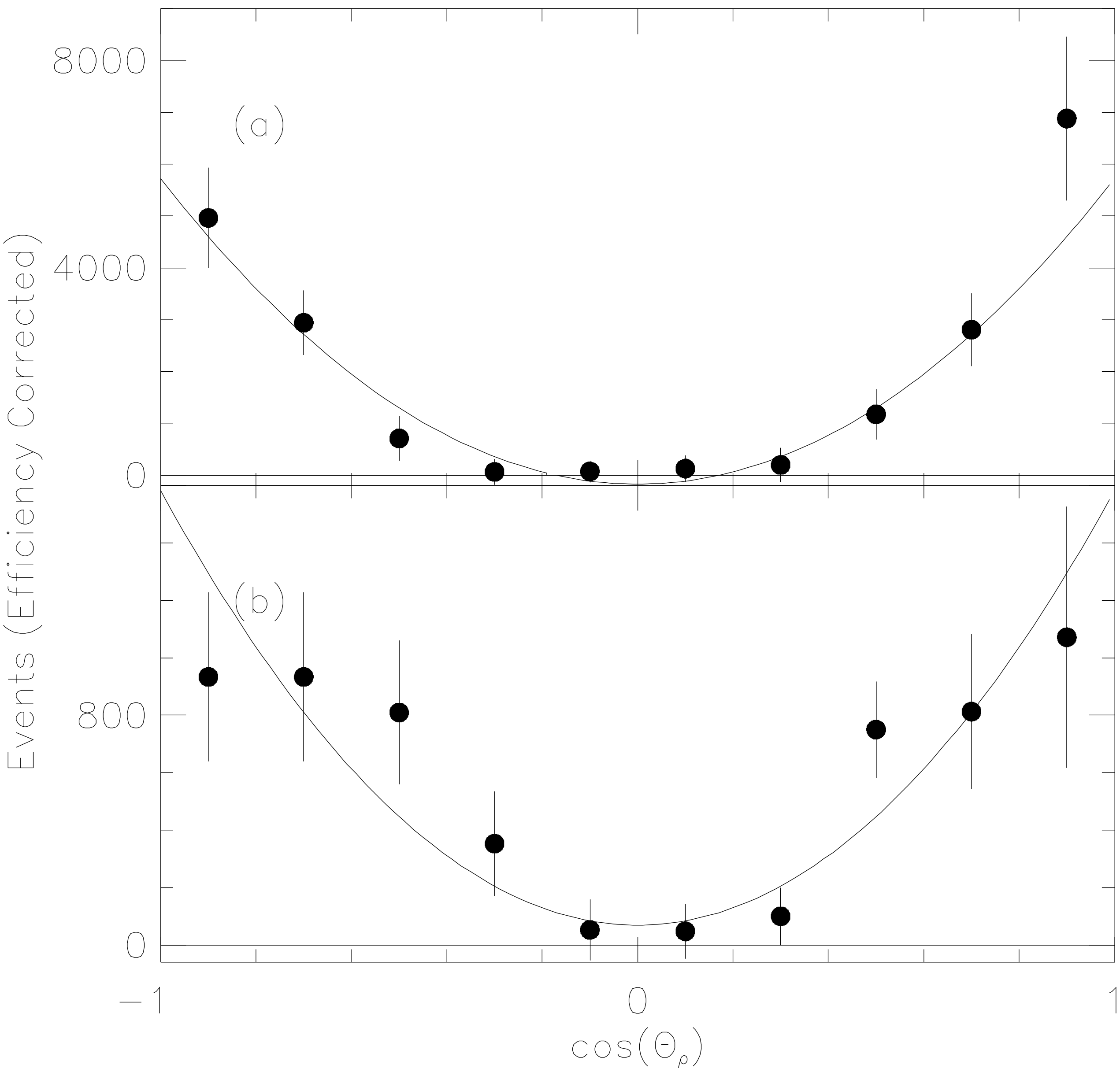

FIG. 6. The efficiency corrected ρ helicity angle distributions: (a) $B^- \to D^0\rho^-$ and (b) $\bar{B}^0 \to D^+\rho^-$ after B mass sideband subtraction.

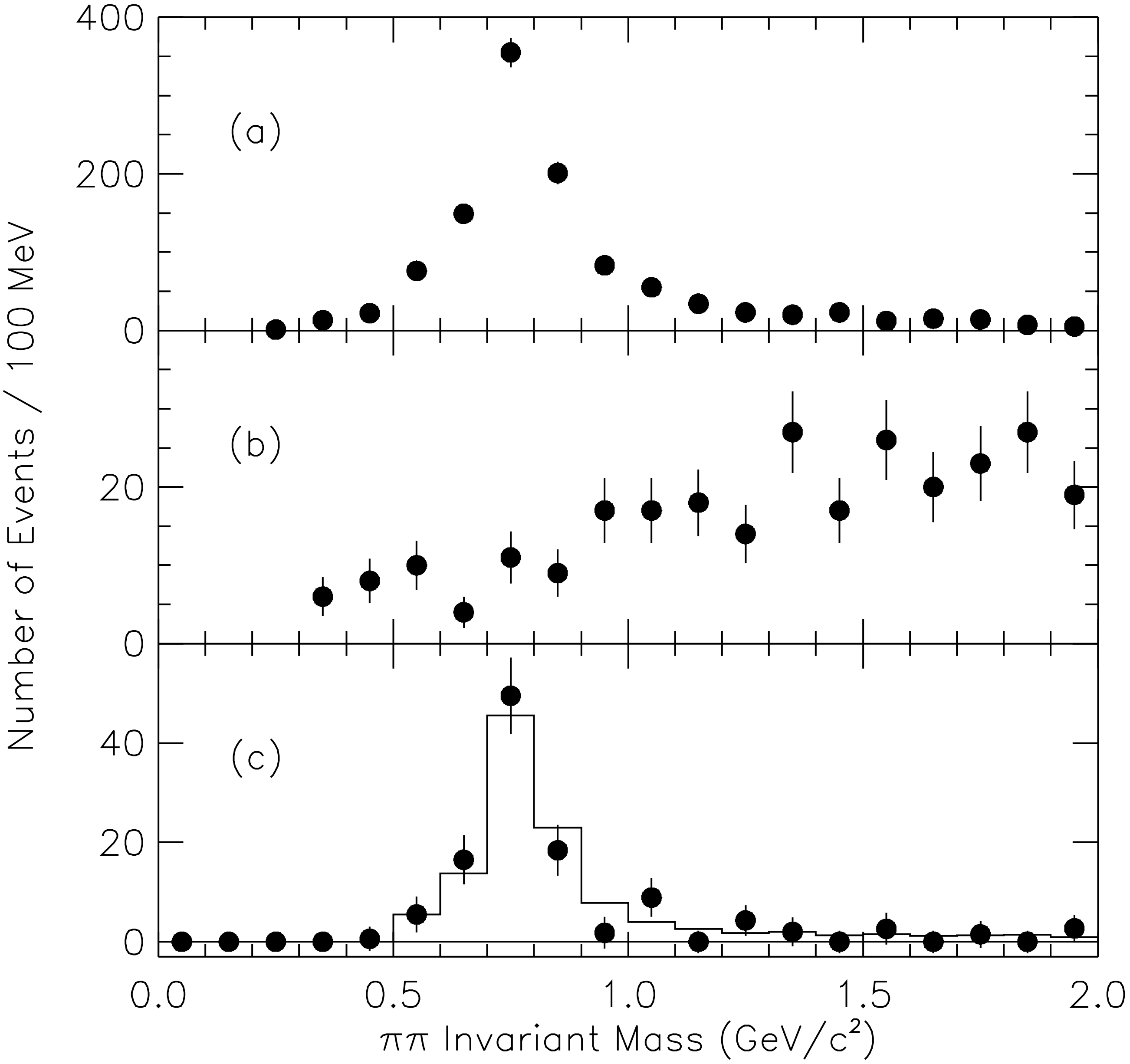

FIG. 7. (a) The $\pi^0\pi^-$ invariant mass spectrum for a $\bar{B}^0 \to D^+\rho^-$ Monte Carlo simulation. (b) The $\pi^0\pi^-$ invariant mass spectrum $\bar{B}^0 \to D^+(\pi^-\pi^0)_{NR}$ Monte Carlo simulation. (c) The $\pi^0\pi^-$ invariant mass spectrum for the $\bar{B}^0 \to D^+\pi^0\pi^-$ mode in data.

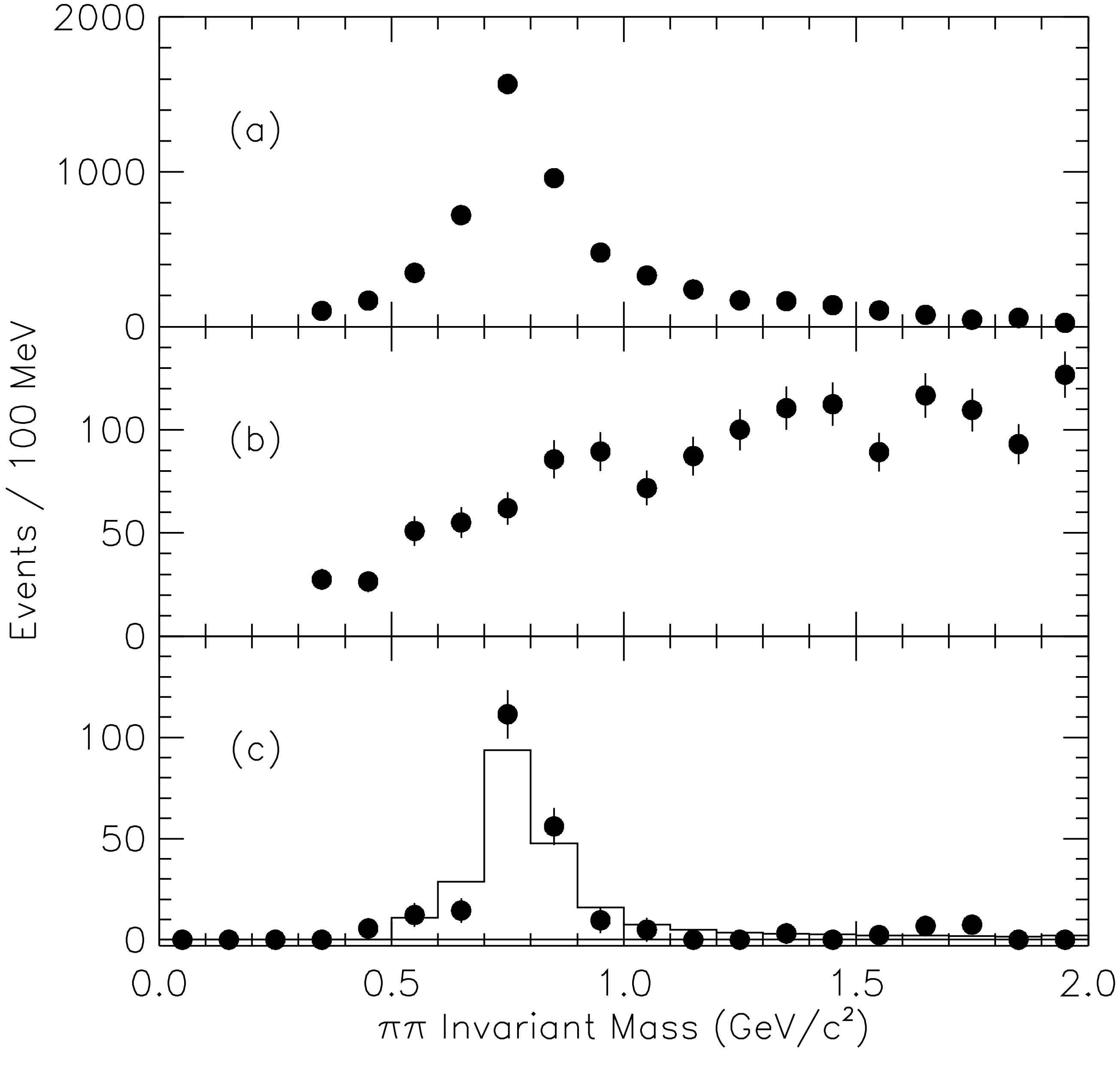

FIG. 8. (a) The $\pi^0\pi^-$ invariant mass spectrum for a $B^- \to D^0\rho^-$ Monte Carlo simulation. (b) The $\pi^0\pi^-$ invariant mass spectrum $B^- \to D^0(\pi^-\pi^0)_{NR}$ Monte Carlo simulation. (c) The $\pi^0\pi^-$ invariant mass spectrum for the $B^- \to D^0\pi^0\pi^-$ mode in data.

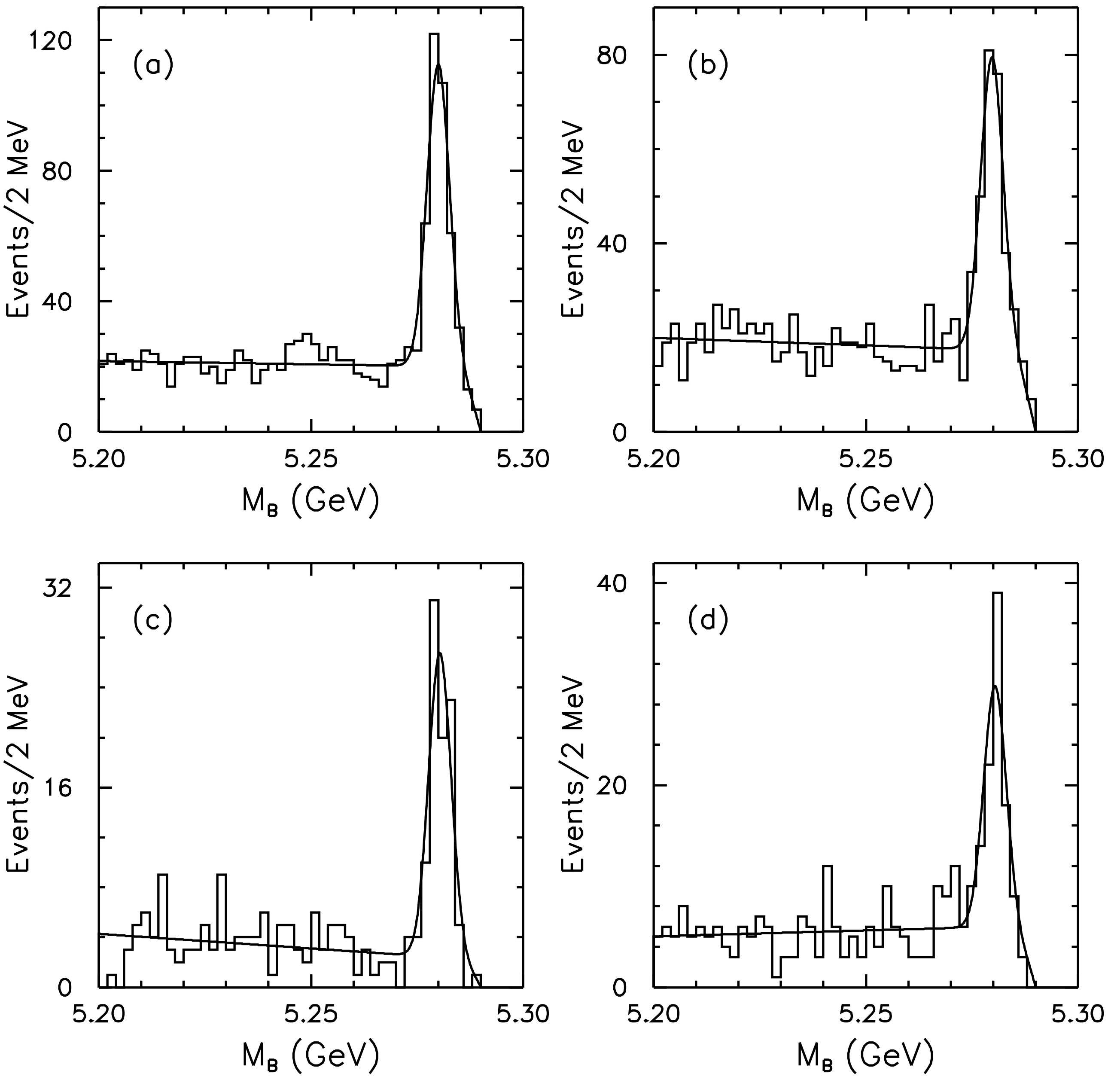

FIG. 9. The beam constrained mass distributions for: (a) $B^- \to D^0\pi^-$, (b) $B^- \to D^0\rho^-$ for $|\cos\Theta_\rho| > 0.4$, (c) $\bar{B}^0 \to D^+\pi^-$ and (d) $\bar{B}^0 \to D^+\rho^-$ for $|\cos\Theta_\rho| > 0.4$.

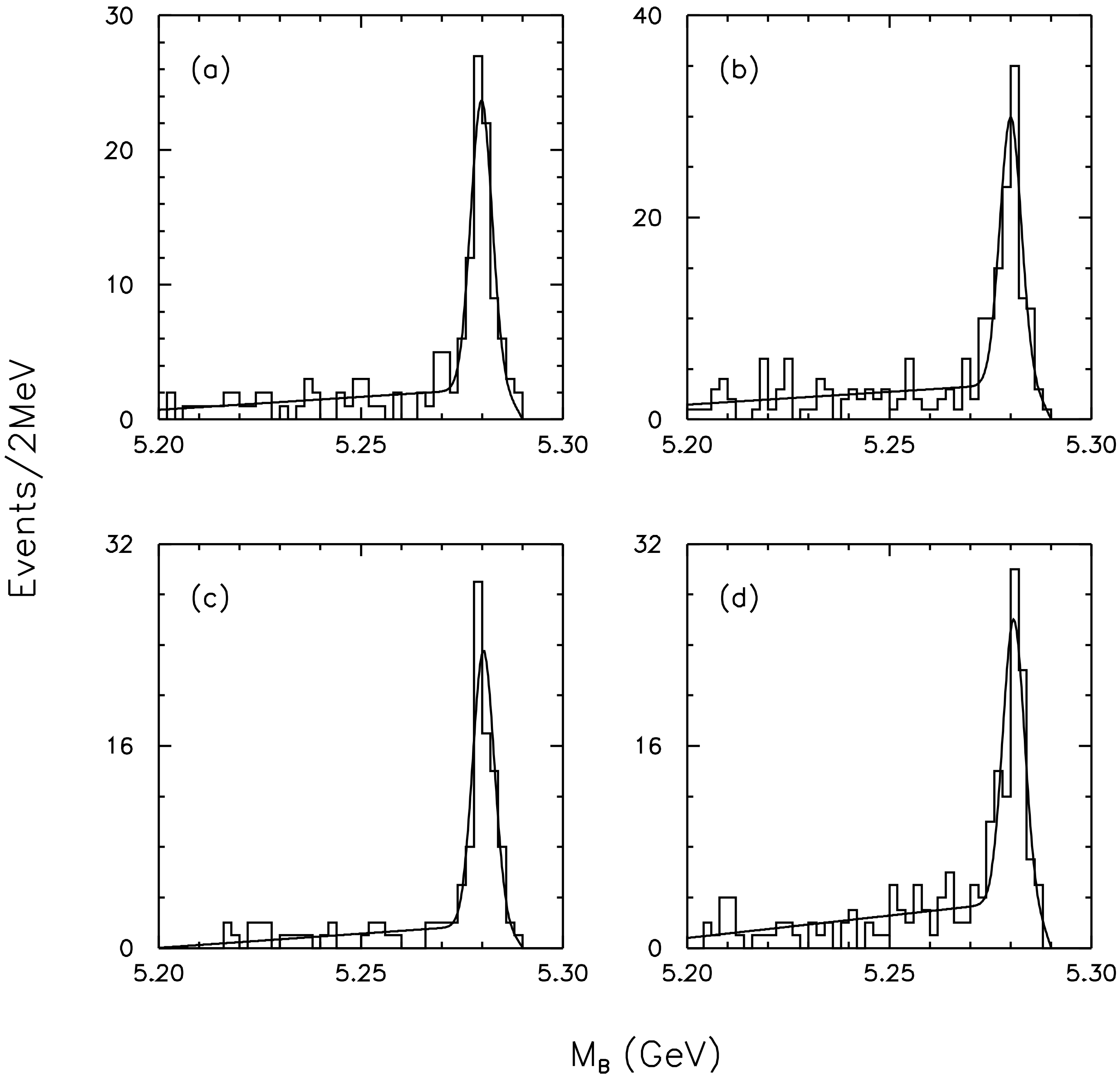

FIG. 10. Beam constrained mass distributions for: (a) $B^- \to D^{*0}\pi^-$, (b) $B^- \to D^{*0}\rho^-$, (c) $\bar{B}^0 \to D^{*+}\pi^-$ and (d) $\bar{B}^0 \to D^{*+}\rho^-$.

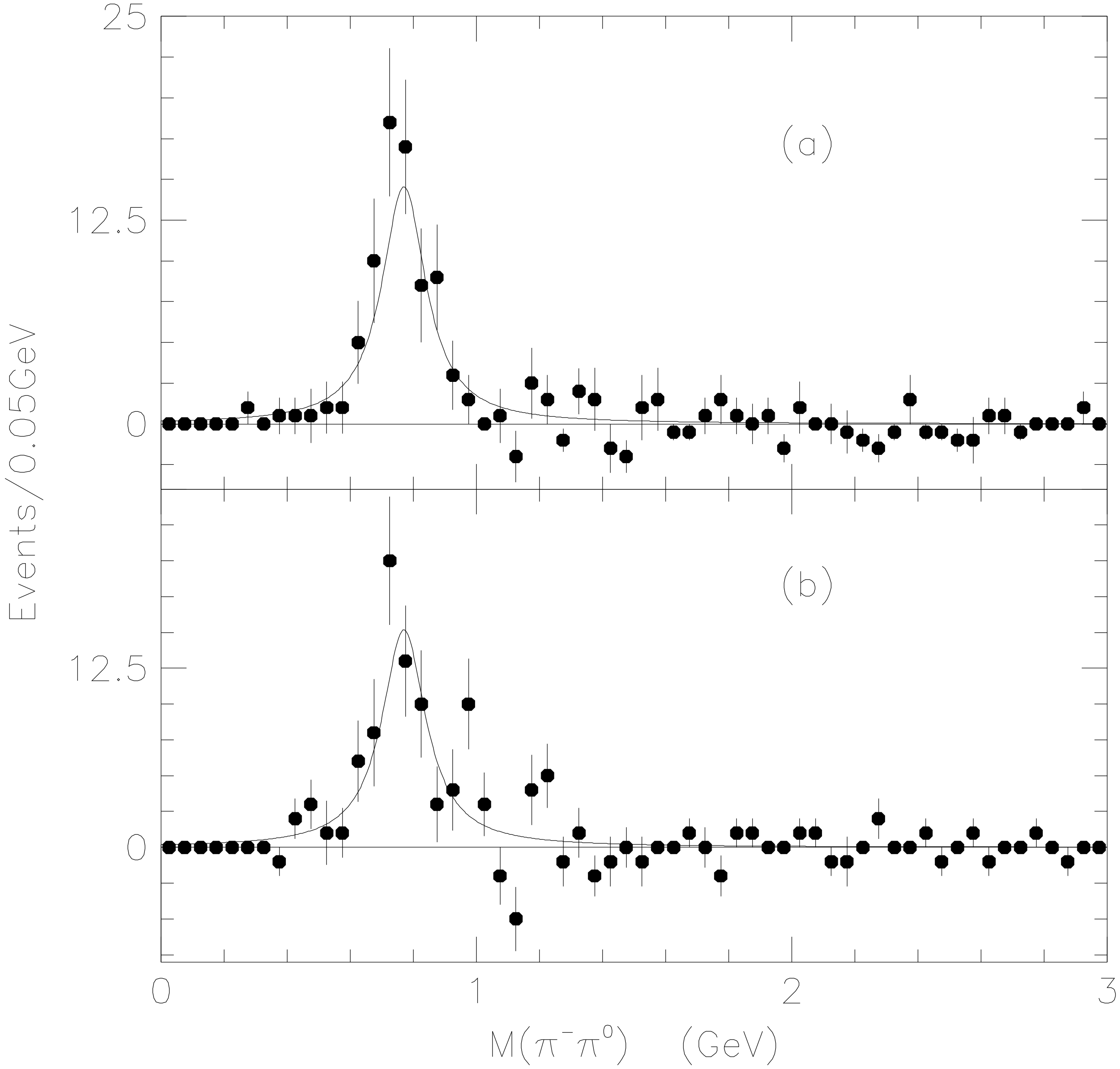

FIG. 11. (a) The $\pi^0\pi^-$ invariant mass spectrum for the $\bar{B}^0 \to D^{*+}\pi^0\pi^-$ decay mode. (b) The $\pi^0\pi^-$ invariant mass spectrum for the $\bar{B}^- \to D^{*0}\pi^0\pi^-$ decay mode.

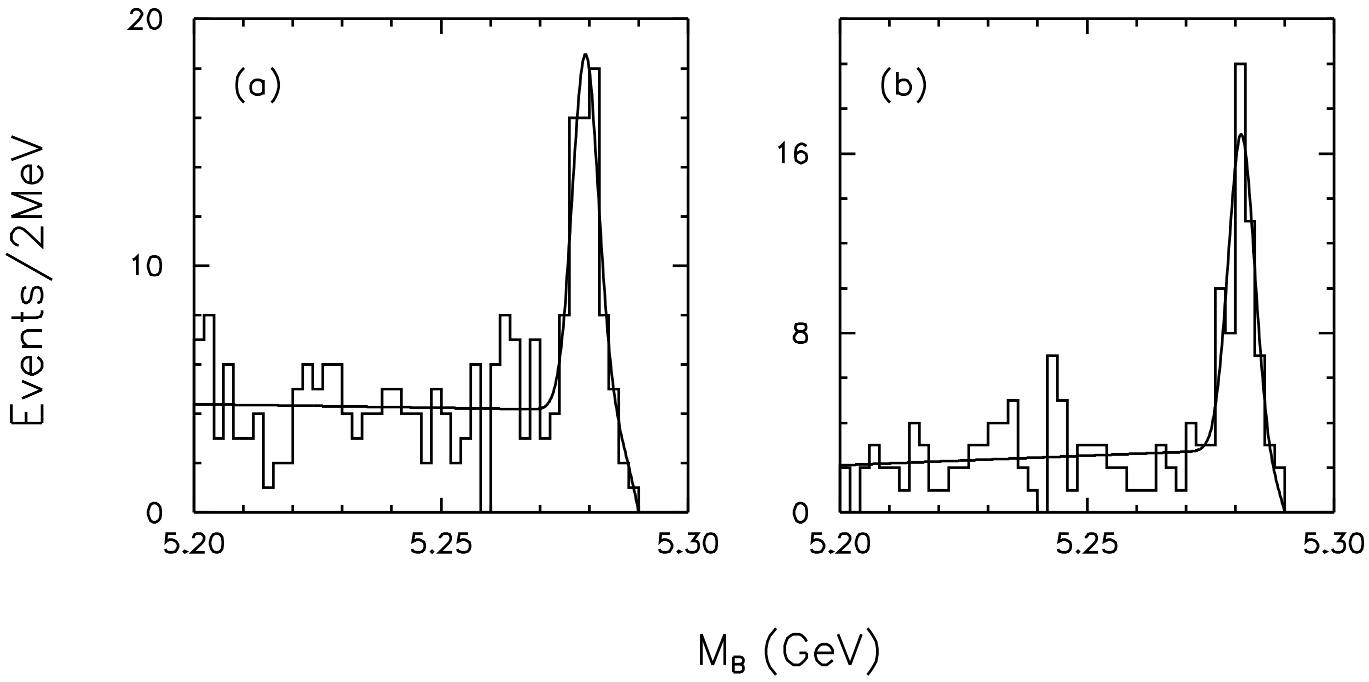

FIG. 12. Beam constrained mass distributions for: (a) $B^- \to D^{*0} a_1^-$ and (b) $\bar{B}^0 \to D^{*+} a_1^-$.

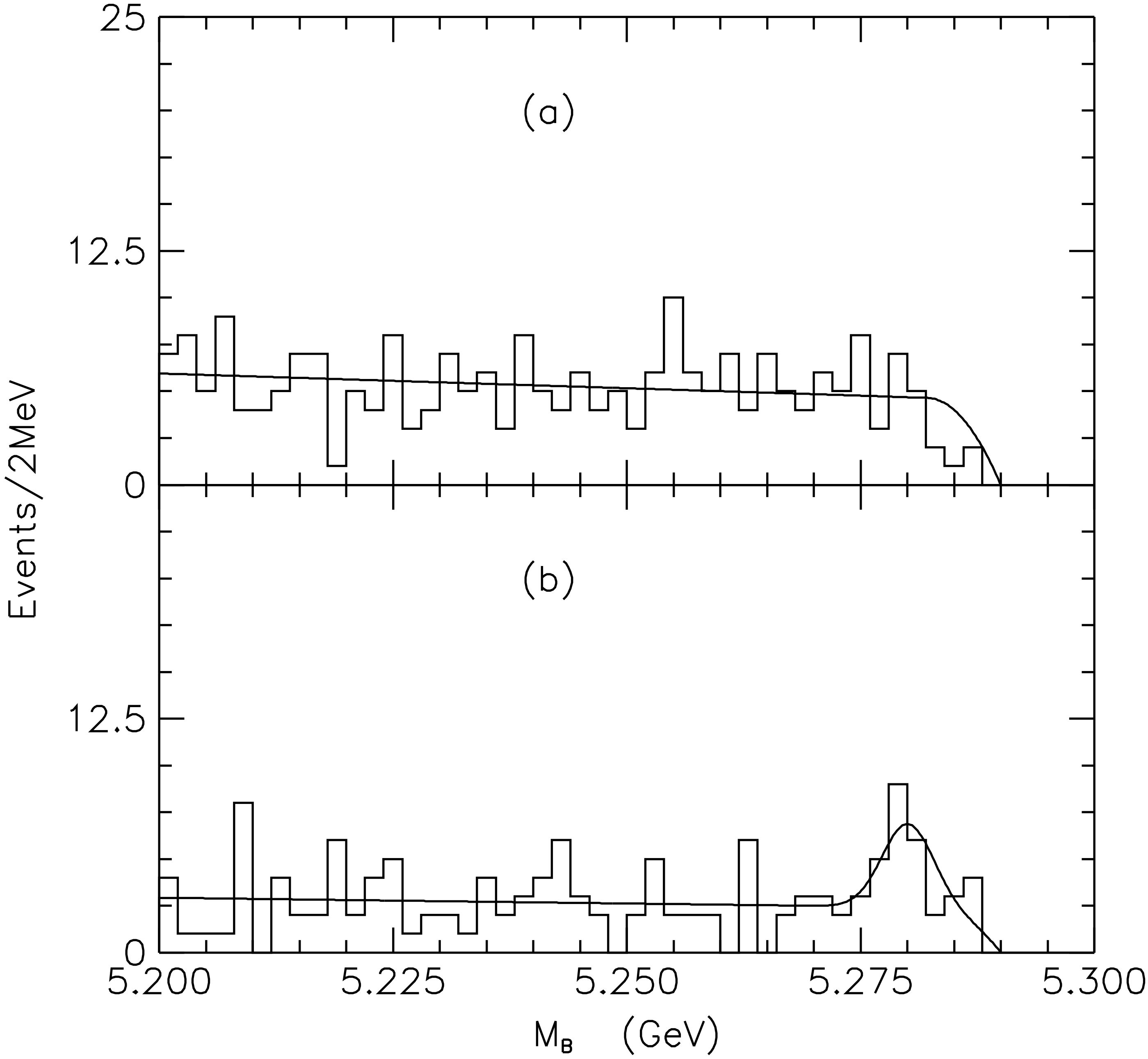

FIG. 13. The M_B distributions for (a) $B^- \to D^{*0}\pi^-\pi^-\pi^+$ and $\bar{B}^0 \to D^{*+}\pi^-\pi^-\pi^+$, where the $\pi^-\pi^-\pi^+$ invariant mass is required to be in the a_1^- mass sidebands.

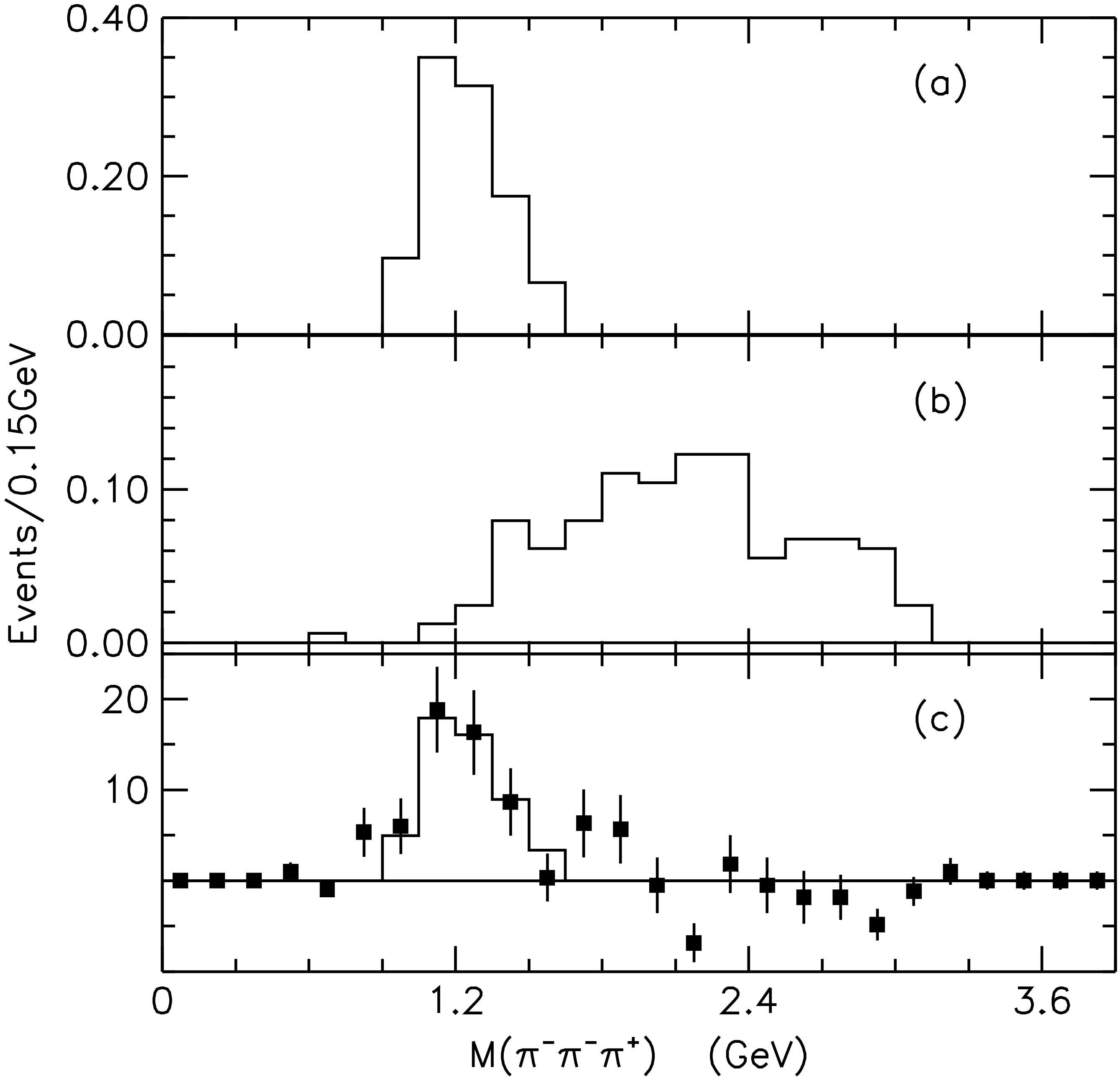

FIG. 14. (a) The $\pi^-\pi^-\pi^+$ invariant mass spectrum from a Monte Carlo simulation of $\bar{B}^0 \rightarrow D^{*+}a_1^-$. (b) The $\pi^-\pi^-\pi^+$ invariant mass spectrum from Monte Carlo simulation for $\bar{B}^0 \rightarrow D^{*+}(\pi^-\rho^0)_{NR}$. (c) The $\pi^-\pi^-\pi^+$ mass spectrum from data after B mass sideband subtraction (points). The fit to the sum of (a) and (b) is superimposed (histogram).

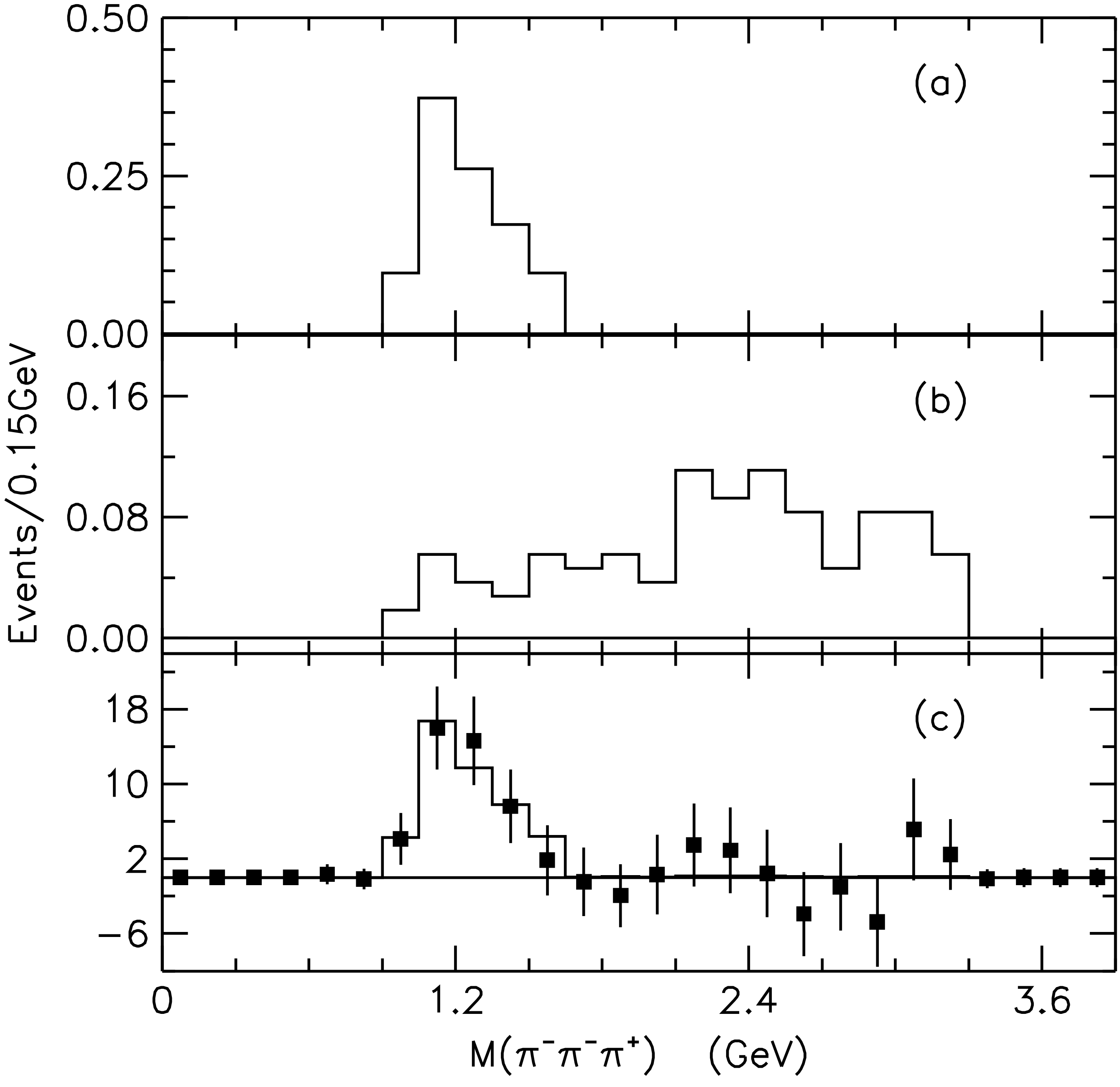

FIG. 15. (a) The $\pi^-\pi^-\pi^+$ invariant mass spectrum from a Monte Carlo simulation of $\bar{B}^- \rightarrow D^{*0}a_1^-$. (b) The $\pi^-\pi^-\pi^+$ invariant mass spectrum from Monte Carlo simulation for $\bar{B}^- \rightarrow D^{*0}(\pi^-\rho^0)_{NR}$. (c) The $\pi^-\pi^-\pi^+$ mass spectrum from data after B mass sideband subtraction (points). The fit to the sum of (a) and (b) is superimposed (histogram).

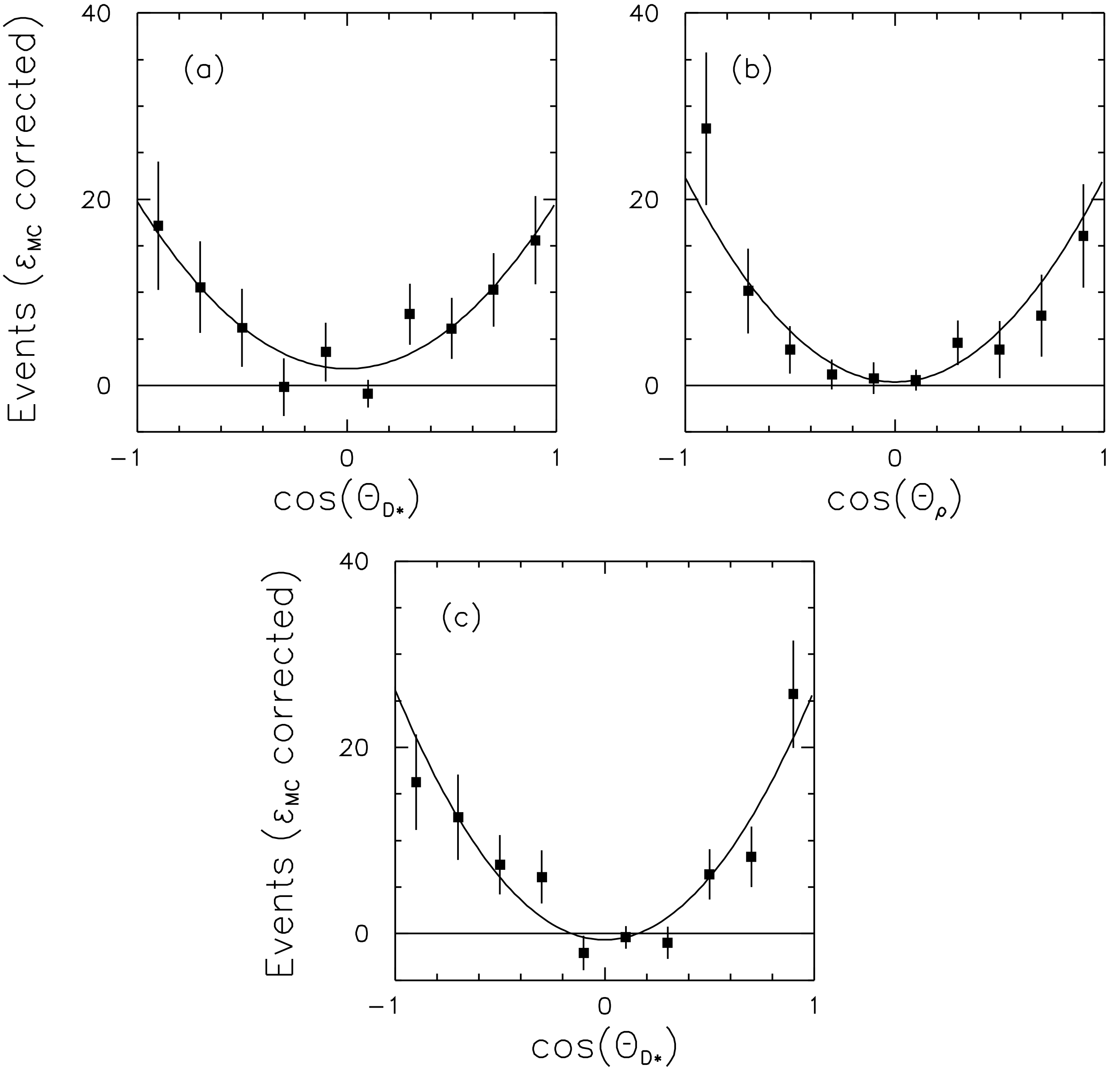

FIG. 16. (a) Helicity angle from $D^{*+} \to D^0\pi^+$ in $\bar{B}^0 \to D^{*+}\rho^-$ and (b)Helicity angle from $\rho^- \to \pi^-\pi^0$ in $\bar{B}^0 \to D^{*+}\rho^-$ (c) Helicity angle from $D^{*+} \to D^0\pi^+$ in $\bar{B}^0 \to D^{*+}\pi^-$. The data have been corrected for efficiency and background subtracted. The curves are the results of the fit described in the text.

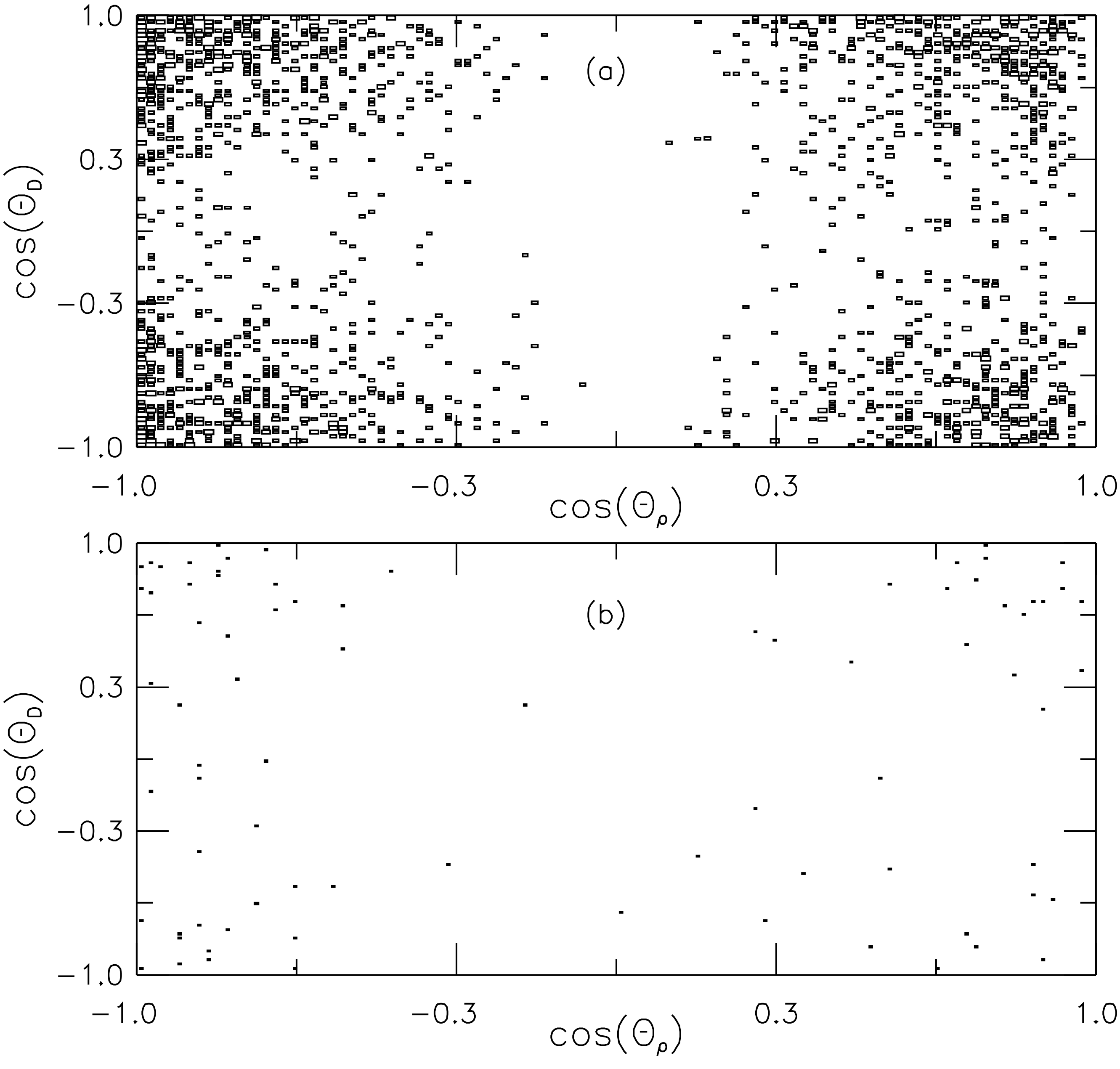

FIG. 17. (a) Monte Carlo simulation of D^{*+} helicity angle versus ρ^- helicity angle for longitudinally polarized $\bar{B}^0 \to D^{*+}\rho^-$. (b) Data for D^{*+} helicity angle versus ρ^- helicity angle for candidates in $\bar{B}^0 \to D^{*+}\rho^-$.

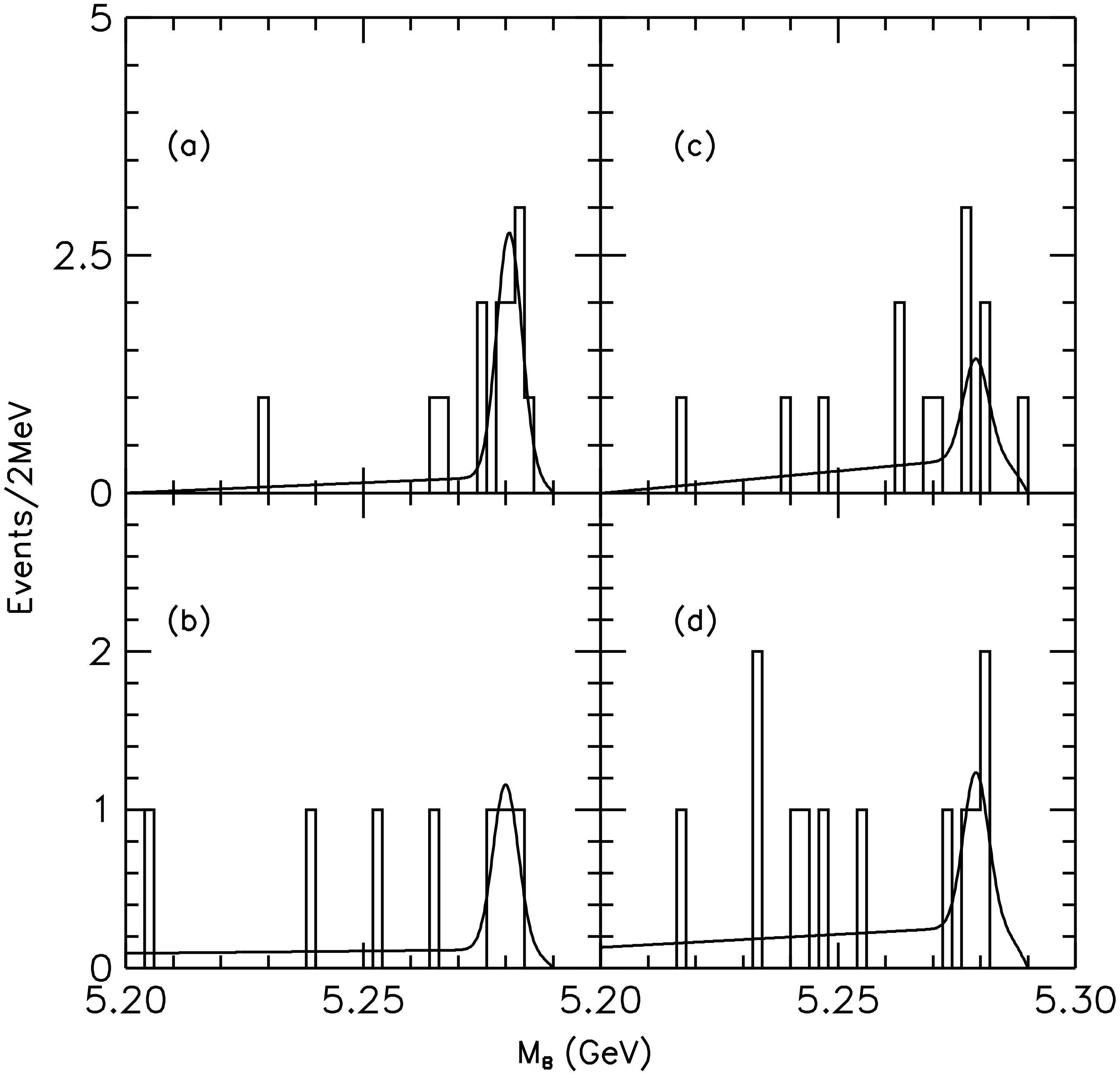

FIG. 18. Beam constrained mass distributions for: (a) $B^- \rightarrow D^{**0}(2420)\pi^-$ where $D^{**0}(2420) \rightarrow D^{*+}\pi^-$, (b) $B^- \rightarrow D^{**0}(2460)\pi^-$ where $D^{**0}(2460) \rightarrow D^{*+}\pi^-$, (c) $B^- \rightarrow D^{**0}(2420)\pi^-\pi^0$ where $D^{**0}(2420) \rightarrow D^{*+}\pi^-$, (d) $B^- \rightarrow D^{**0}(2460)\pi^-\pi^0$ where $D^{**0}(2460) \rightarrow D^{*+}\pi^-$

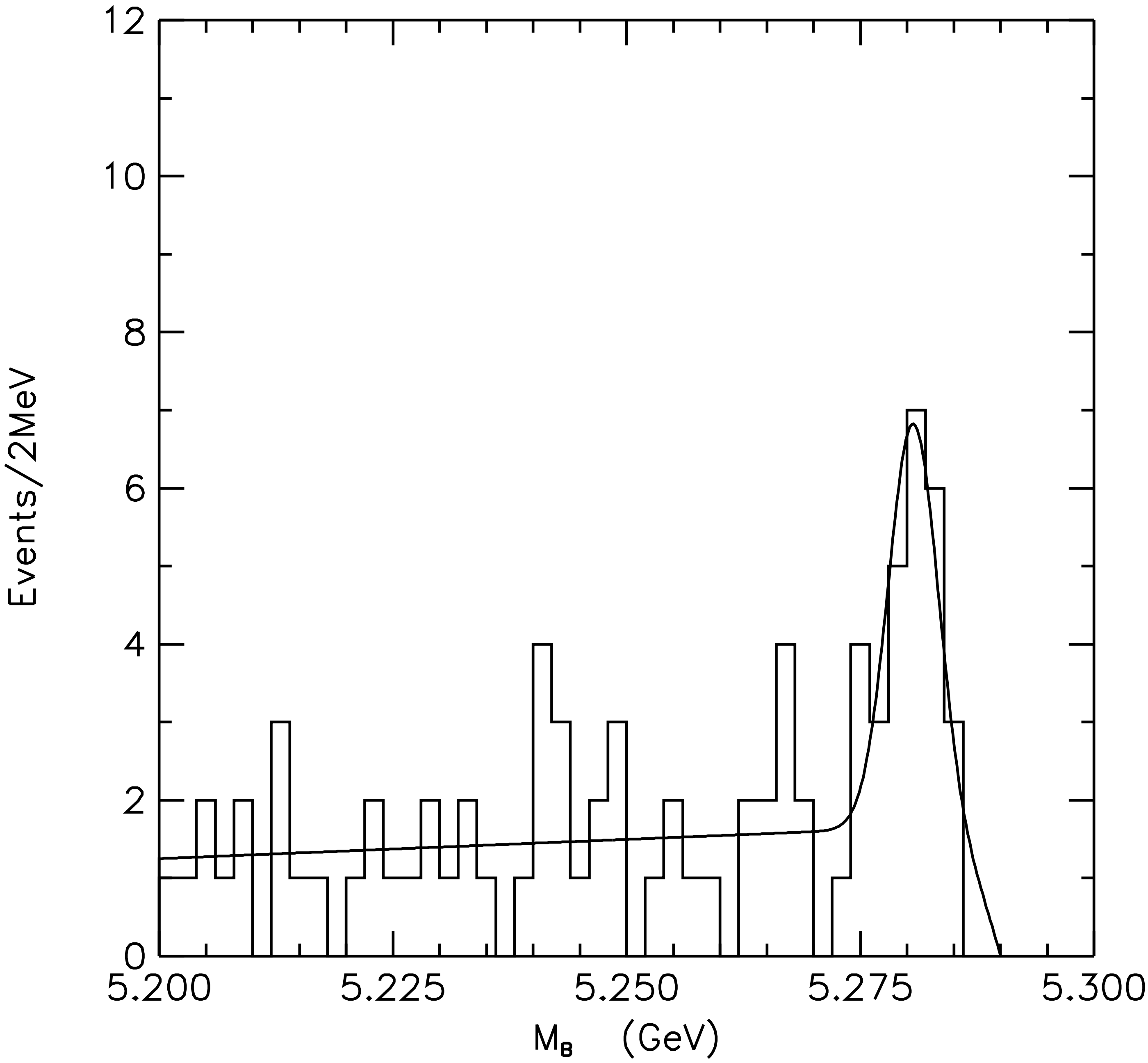

FIG. 19. Beam constrained mass distribution for $B^- \to D^{*+}\pi^-\pi^-$

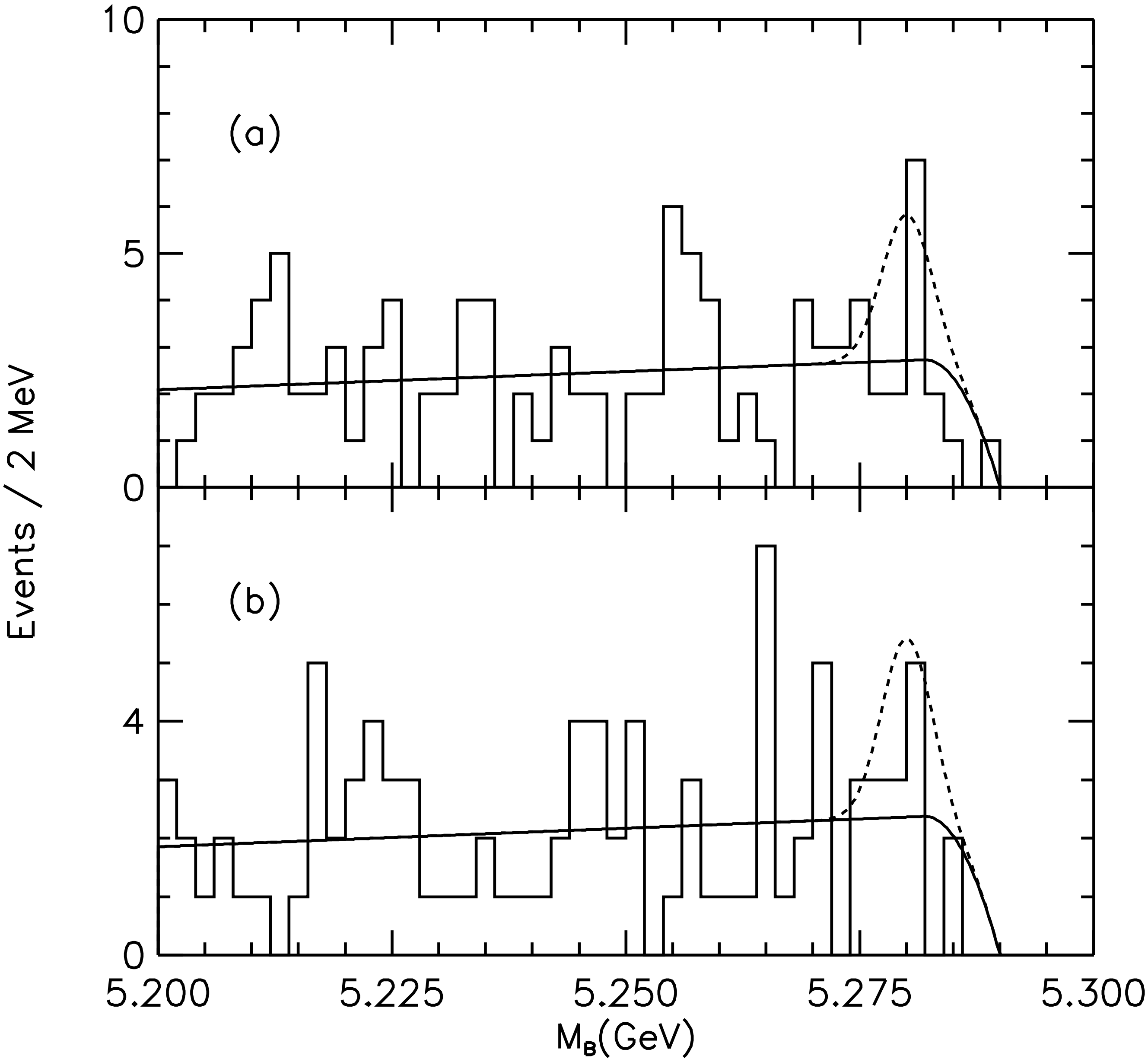

FIG. 20. Beam constrained mass distributions for: (a) $B^- \to D^+\pi^-\pi^-$ and (b) $\bar{B}^0 \to D^0\pi^-\pi^+$. The curve is the result of the fit and the dotted line is the 90% confidence level upper limit.

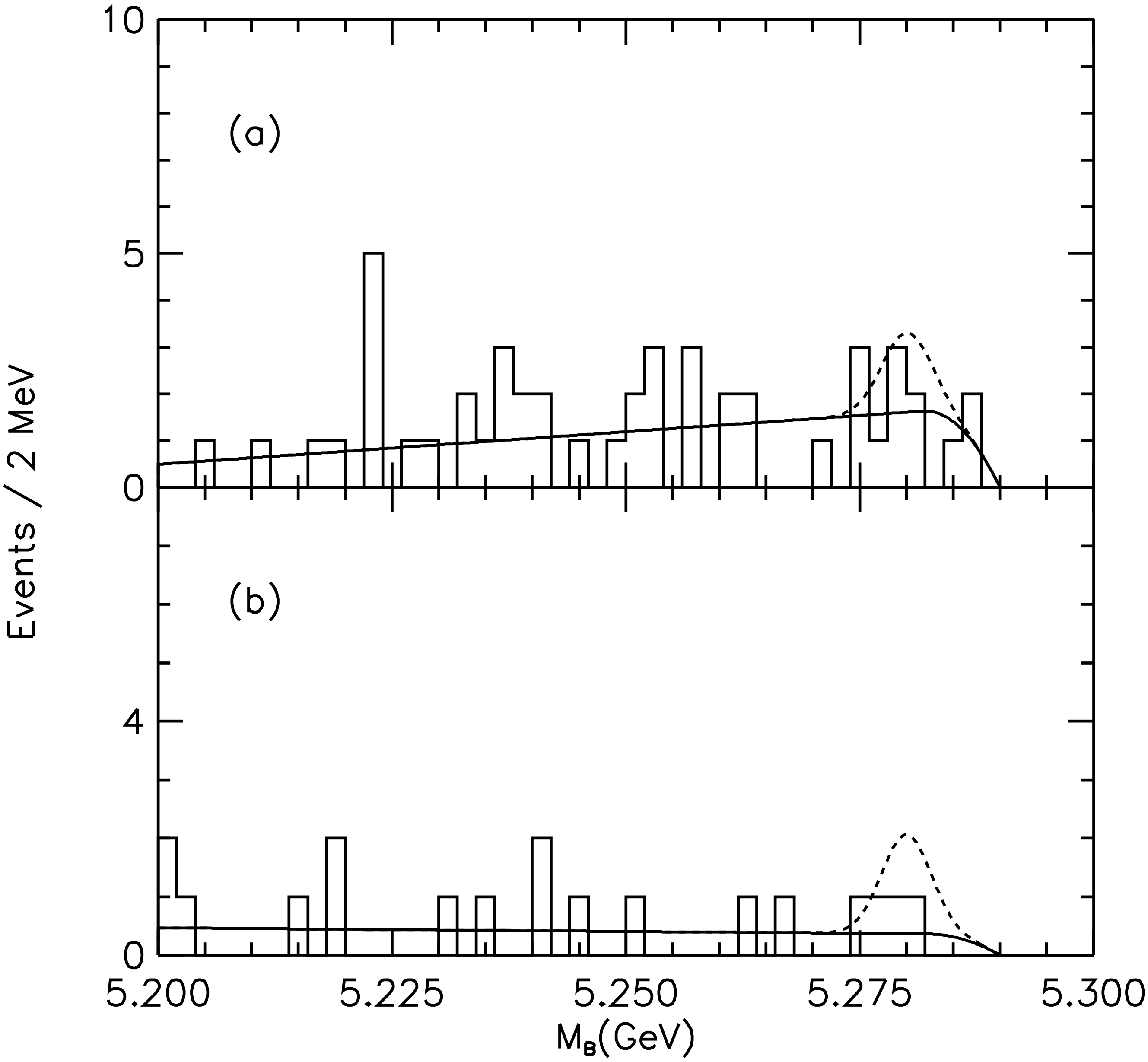

FIG. 21. Beam constrained mass distributions for: (a) $B^- \rightarrow D^{**0}(2460)\pi^-$ where $D^{**0}(2460) \rightarrow D^+\pi^-$, and (b) $\bar{B}^0 \rightarrow D^{**+}(2460)\pi^-$ where $D^{**+}(2460) \rightarrow D^0\pi^+$. The curve is the result of the fit and the dotted line is the 90% confidence level upper limit.

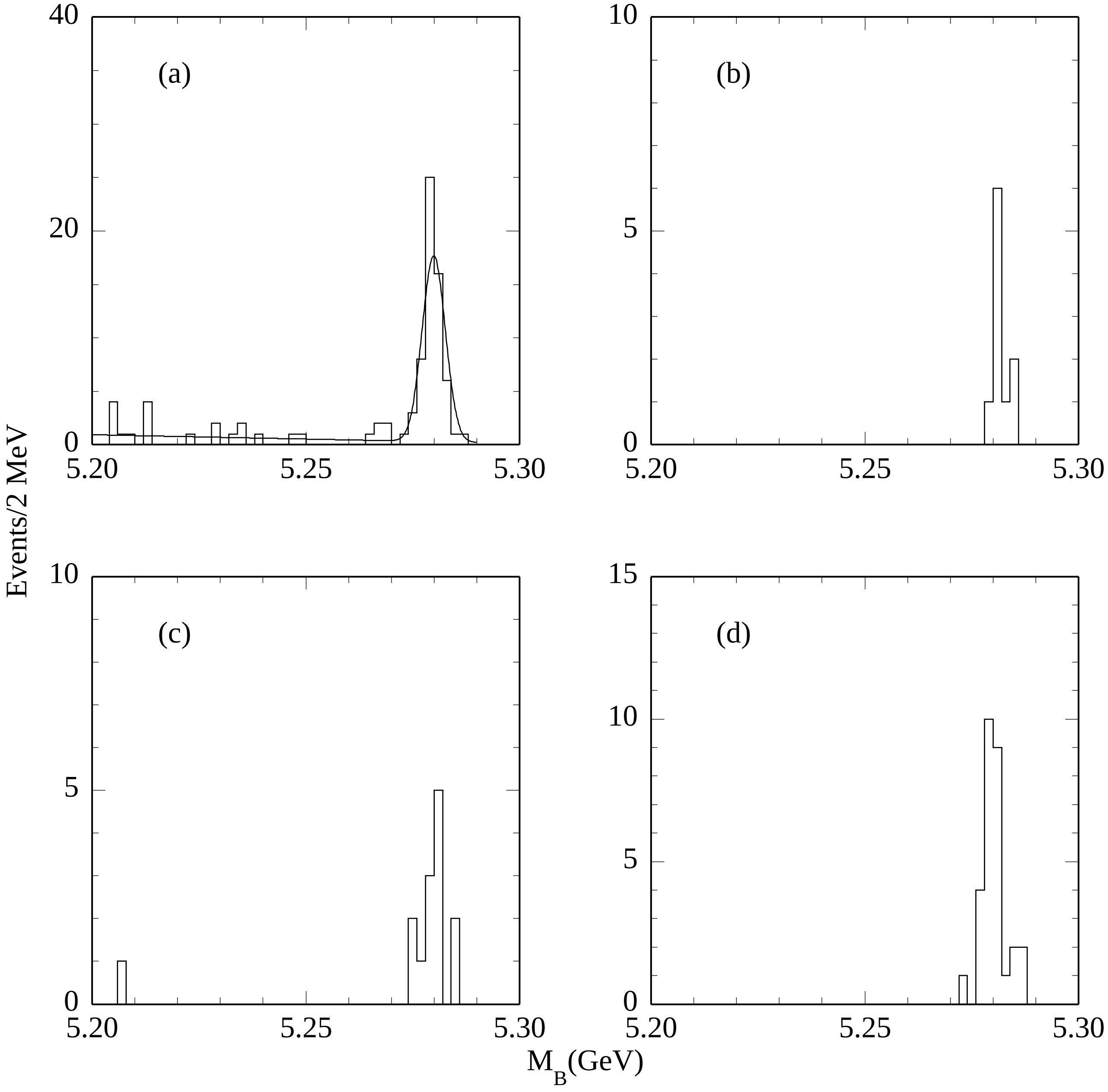

FIG. 22. Beam-constrained mass for: (a) $B^- \to \psi K^-$, (b) $\bar{B}^0 \to \psi \bar{K}^0$, (c) $B^- \to \psi \bar{K}^{*-}$, and (d) $\bar{B}^0 \to \psi K^{*0}$.

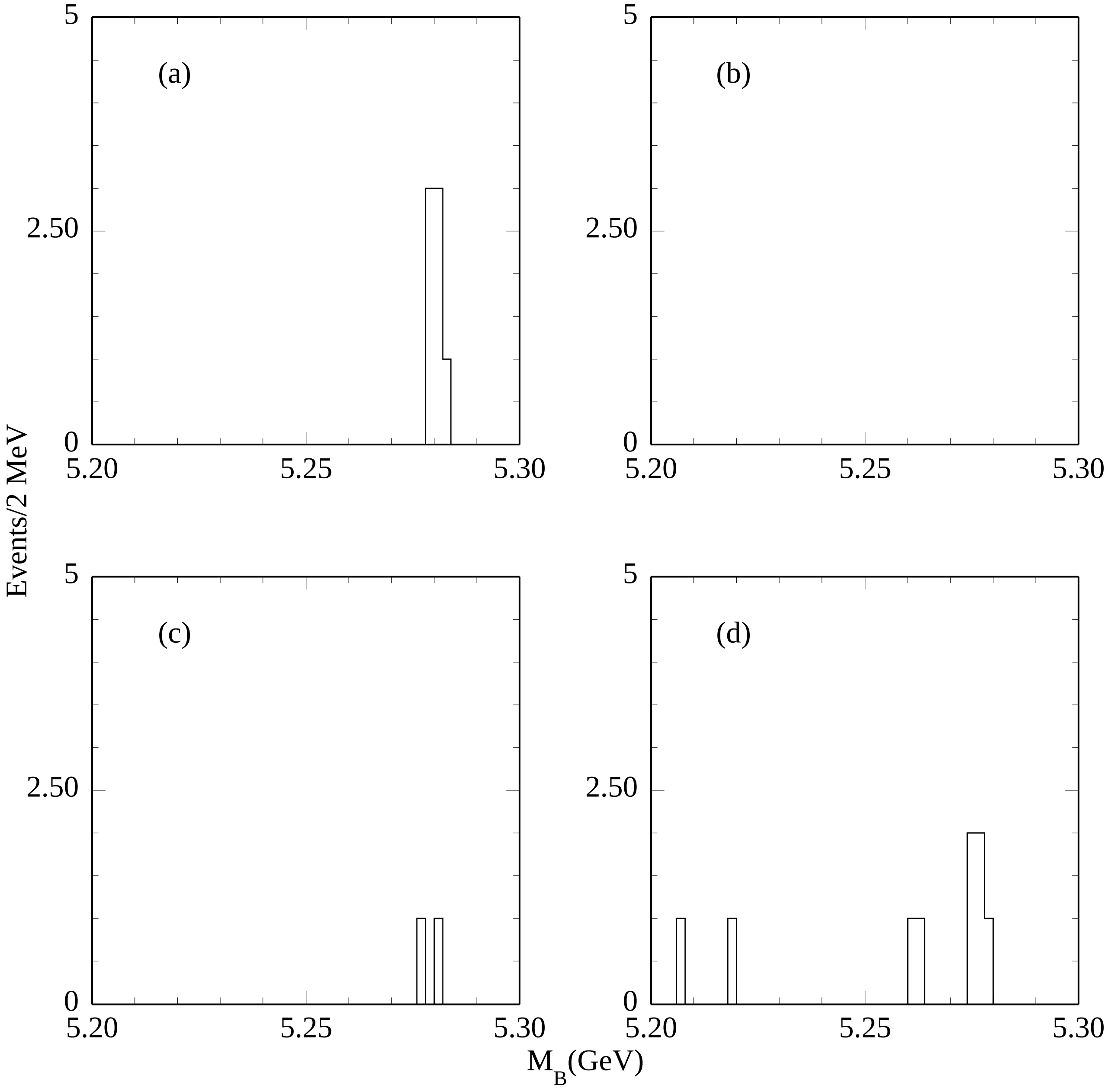

FIG. 23. Beam-constrained mass for: (a) $B^- \to \psi' K^-$, (b) $\bar{B}^0 \to \psi' \bar{K}^0$, (c) $B^- \to \psi' \bar{K}^{*-}$, and (d) $\bar{B}^0 \to \psi' K^{*0}$.

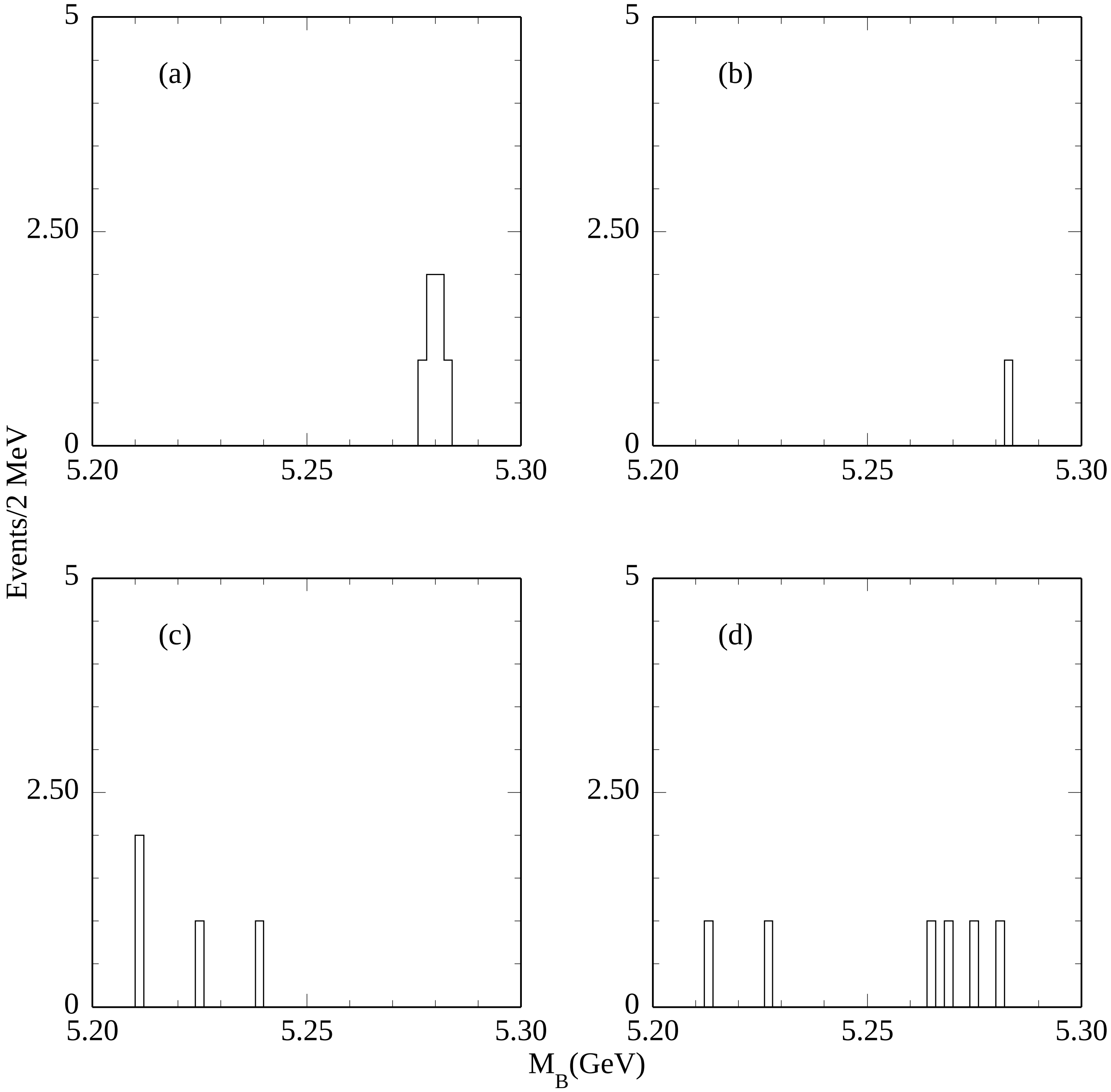

FIG. 24. Beam-constrained mass for: (a) $B^- \rightarrow \chi_{c1} K^-$, (b) $\bar{B^0} \rightarrow \chi_{c1} \bar{K^0}$, (c) $B^- \rightarrow \chi_{c1} K^{*-}$, and (d)$\bar{B^0} \rightarrow \chi_{c1} \bar{K}^{*0}$.

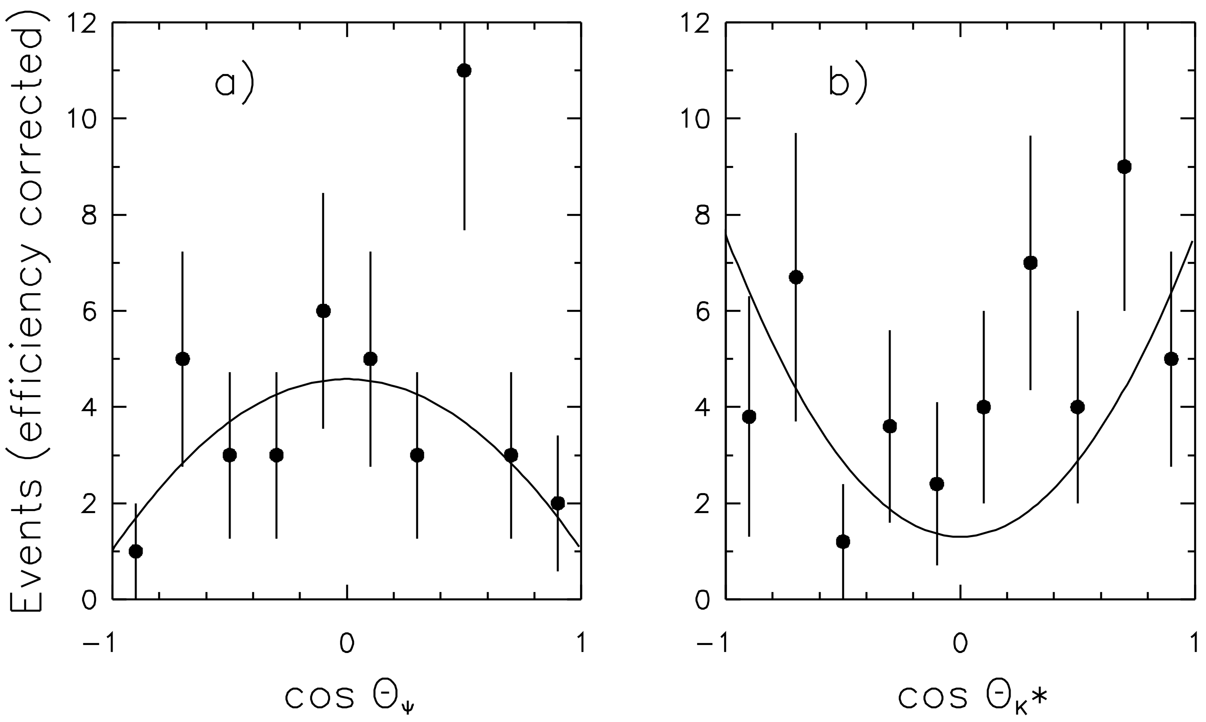

FIG. 25. Distribution of (a) the ψ and (b) the K^* efficiency corrected helicity distributions in $B \to \psi K^*$ decays. The overlaid curves are projections of the unbinned maximum likelihood fit described in the text.

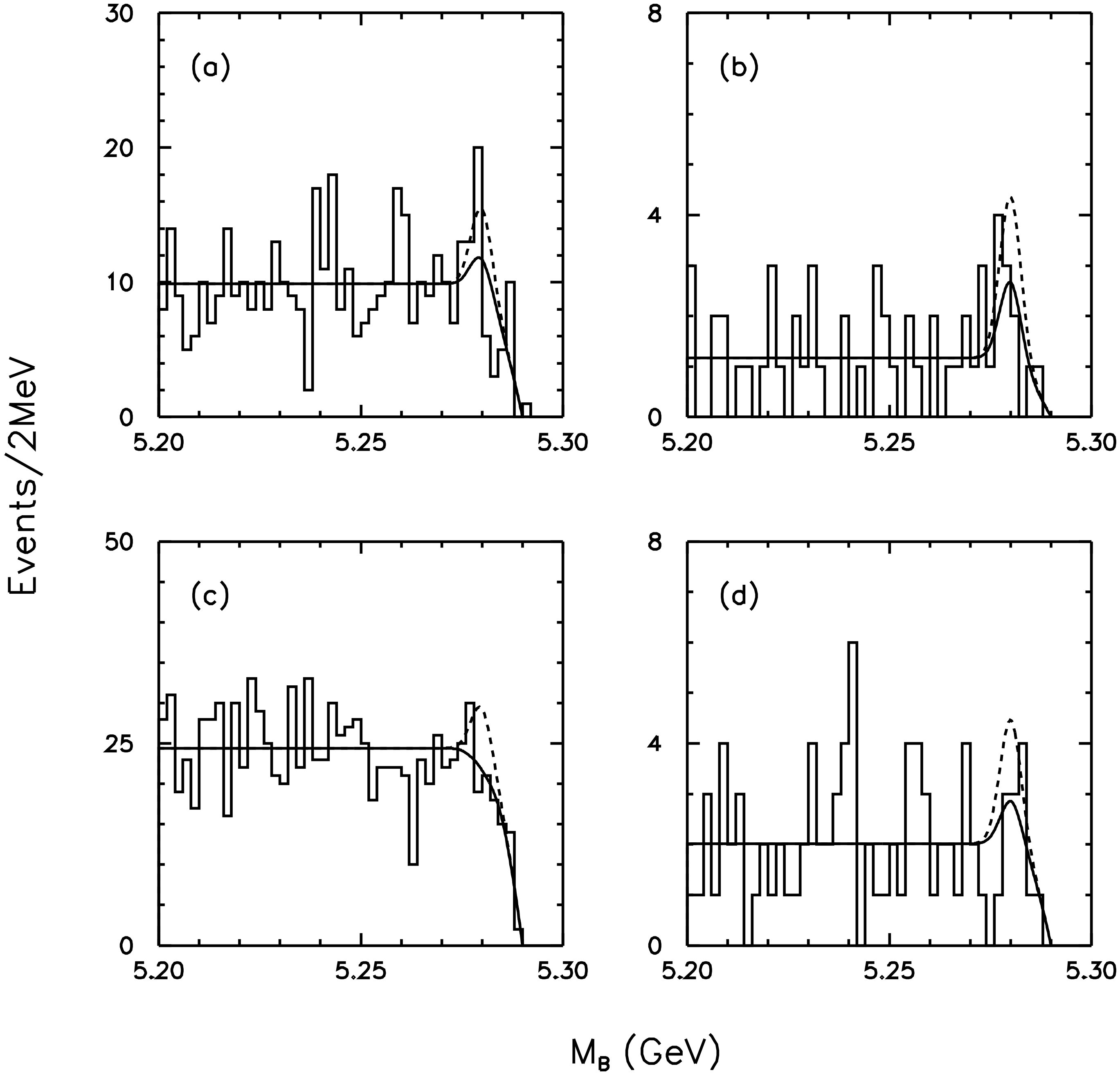

FIG. 26. Beam constrained mass distributions for: (a) $\bar{B}^0 \to D^0\pi^0$, (b) $\bar{B}^0 \to D^{*0}\pi^0$, (c) $\bar{B}^0 \to D^0\rho^0$, and (d) $\bar{B}^0 \to D^{*0}\rho^0$. The curves are the results of a fit with the CLEO background shape. The dotted lines show the the 90% C.L. upper limit.

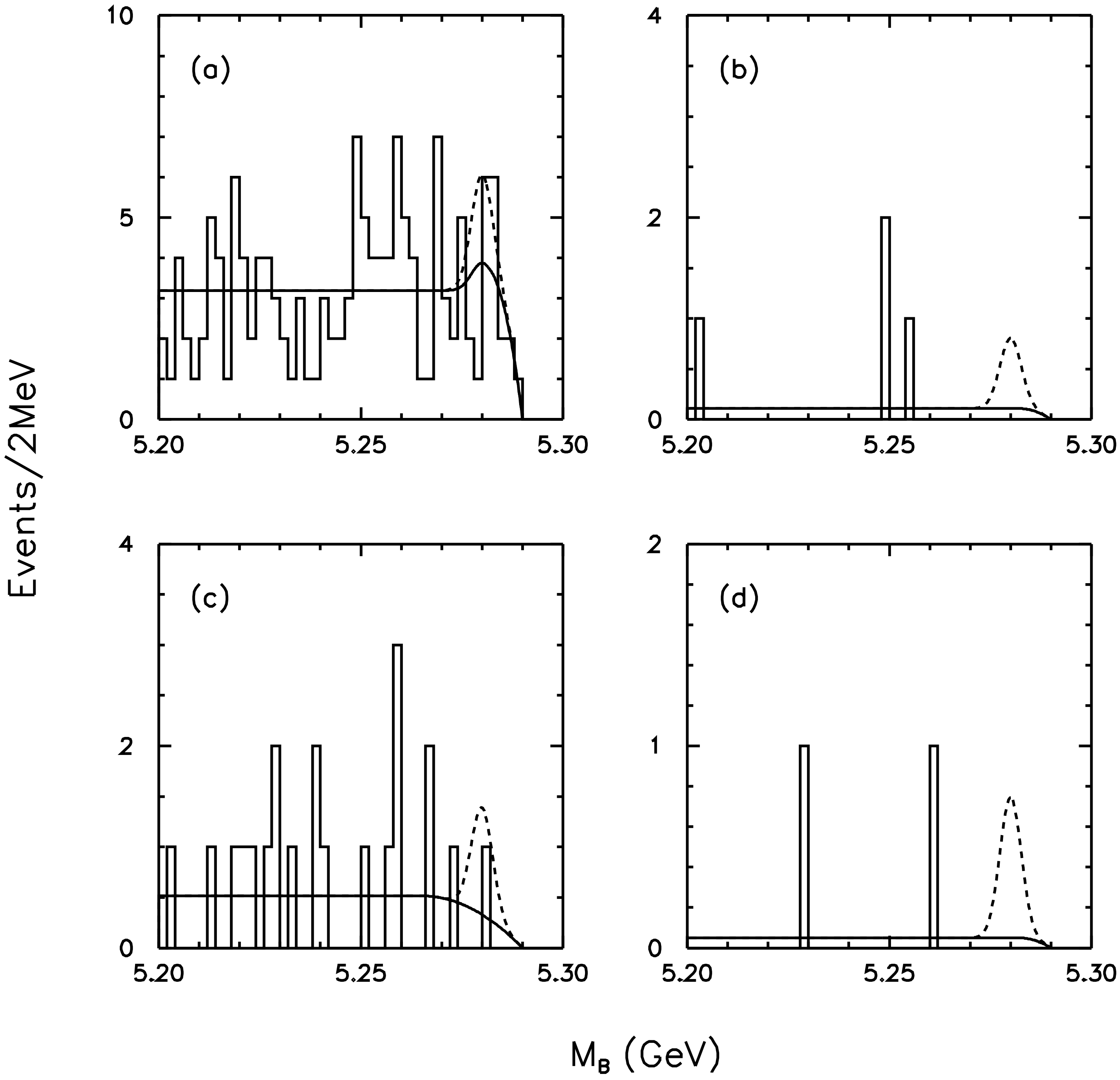

FIG. 27. Beam constrained mass distributions for: (a) $\bar{B}^0 \to D^0\eta$, (b) $\bar{B}^0 \to D^{*0}\eta$, (c) $\bar{B}^0 \to D^0\eta'$, and (d) $\bar{B}^0 \to D^{*0}\eta'$. The curves are the results of a fit with the CLEO background shape. The dotted lines show the the 90% C.L. upper limit.

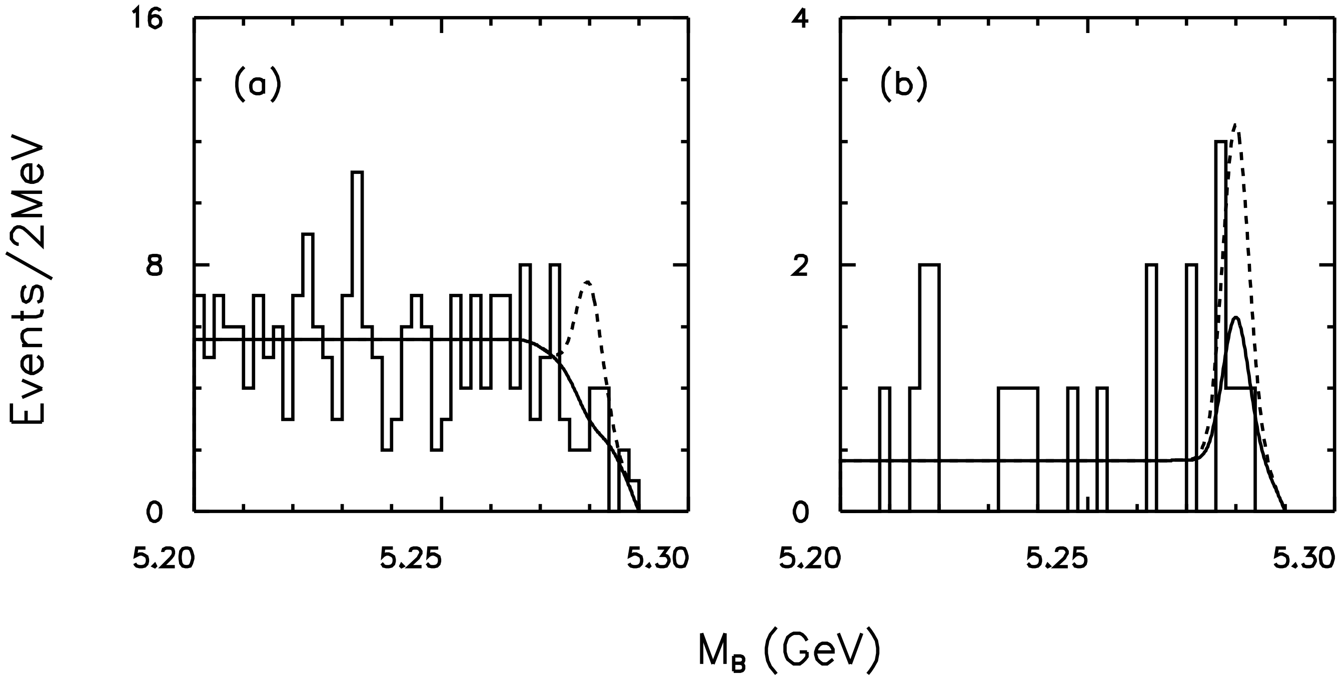

FIG. 28. Beam constrained mass distributions for: (a) $\bar{B}^0 \to D^0\omega$ and (b) $\bar{B}^0 \to D^{*0}\omega$. The curves are the results of the fit. The dotted lines show the the 90% C.L. upper limit.

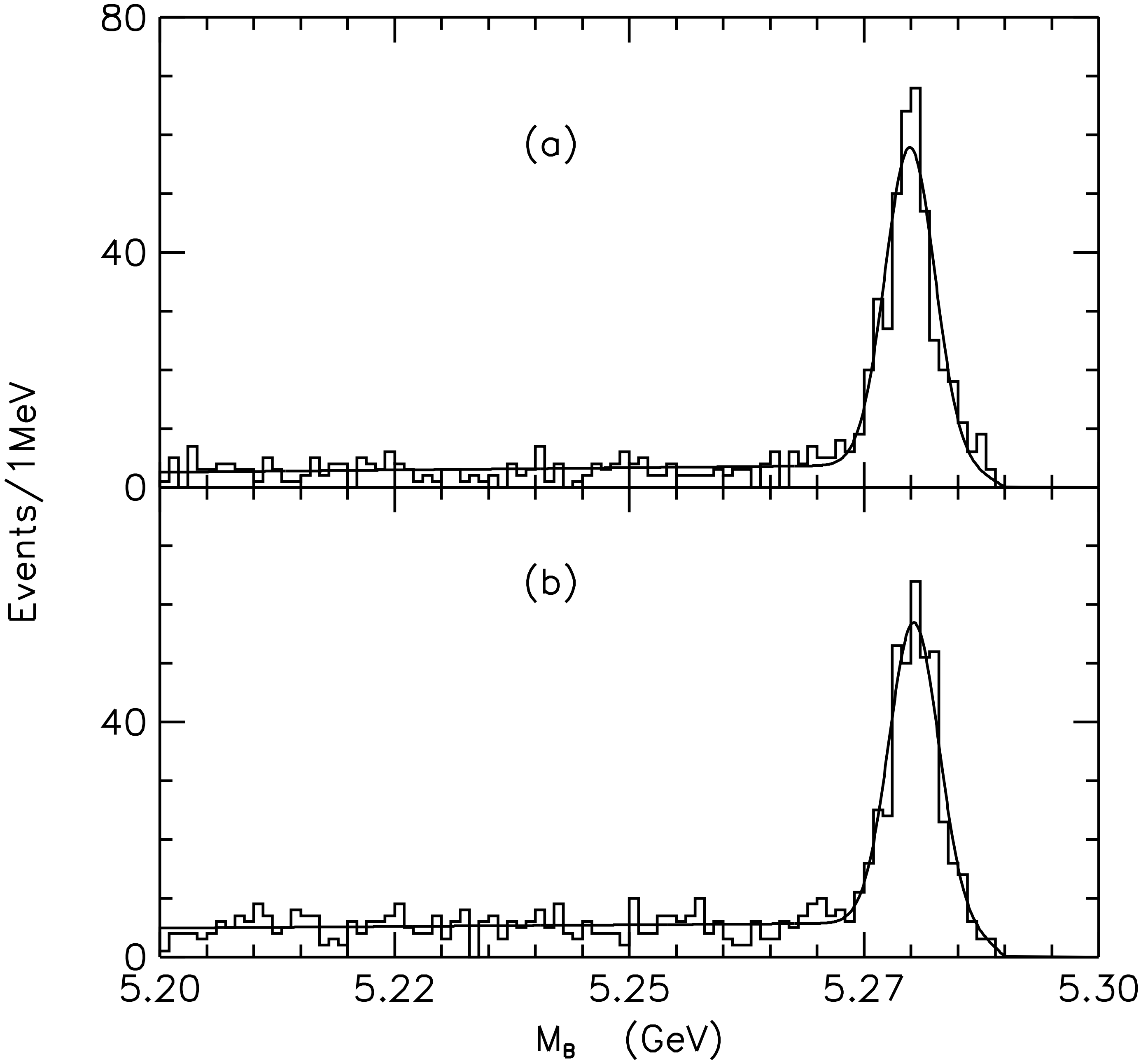

FIG. 29. M_B for (a) B^- events and (b) $\bar{B}^0$ events.

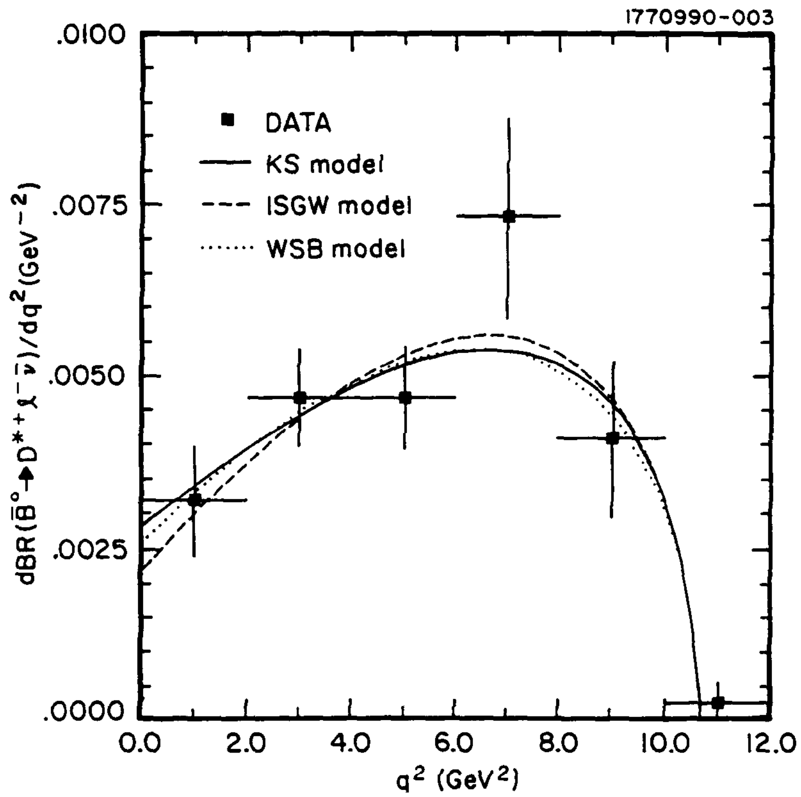

FIG. 30. The Q^2 distribution for the decay $\bar{B}^0 \to D^{*+}\ell^-\bar{\nu}_\ell$. This is a weighted average from CLEO and ARGUS data. The curves are fits using various models of semileptonic decays (from Ref. [51]).

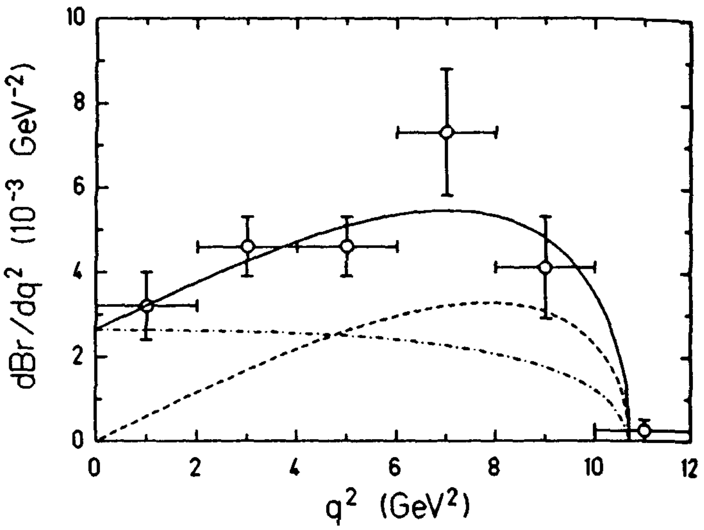

FIG. 31. The differential branching ratio for $\bar{B}^0 \to D^{*+}\ell\bar{\nu}_\ell$. The curves show the theoretical prediction for producing transversely (dashed) and longitudinally (dash-dotted) polarized D^* mesons, as well as the total decay rate (solid) (from Ref. [60]).